[American Journal of Science, Vol. 308, June, 2008, P. 727–769, DOI 10.2475/06.2008.01]

American Journal of Science

JUNE 2008

UTURUNCU VOLCANO, BOLIVIA: VOLCANIC UNREST DUE TO MID-CRUSTAL MAGMA INTRUSION

R. STEPHEN J. SPARKS*,†, CHRIS B. FOLKES*,**, MADELEINE C.S. HUMPHREYS*,***, DANIEL N. BARFOD§, JORGE CLAVERO§§, MAYEL C. SUNAGUA§§§, STEPHEN R. McNUTT‡, and MATTHEW E. PRITCHARD‡‡

ABSTRACT. Uturuncu volcano, SW Bolivia, is a dormant stratovolcano (~85 km^3) dominated by dacitic lava domes and flows. $^{39}Ar/^{40}Ar$ ages show that the volcano was active between 890 ka and 271 ka, with the lavas becoming younger and less extensive at higher elevations. There are current signs of unrest. Between 1992 and 2006 geodetic satellite measurements record an ongoing 70 km deformation field with a central uplift rate of 1 to 2 cm/yr. Deformation indicates volume changes of 400 x 10^8 m^3 over 14 years, an average of ~1 m^3/s (10^{-2} km^3/yr). The deformation is attributed to magma intrusion into the Altiplano-Puna regional crustal magma body. Deformation models indicate a source at depths of 17 to 30 km beneath current local relief. In a reconnaissance survey, persistent seismic activity (mean of 2.6 earthquakes per hour with a maximum of 14 per hour) was recorded at about 4 km depth below the center of the uplift, 4 km SW of the volcano's summit. The seismic events have a normal b value (~1.04) and activity is attributed to brittle deformation in the elastic crust above the active deep magma intrusion. The porphyritic dacite lavas (64–68% SiO_2) have a plagioclase-orthopyroxene-biotite-magnetite-ilmenite assemblage and commonly contain juvenile silicic andesite inclusions, cognate norite nodules and crustal xenoliths. Temperature estimates are in the range 805 to 872°C for the dacites and about 980°C for the silicic andesites. The dacite magmas formed by fractional crystallization of andesite forming norite cumulates and involving partial melting of crust. Compositions and zoning patterns of orthopyroxene and plagioclase phenocrysts indicate that compositional variation in the dacites is caused by magma mixing with the silicic andesite. Reversely zoned orthopyroxene phenocrysts in the andesitic end-member are explained by changing oxidation states during crystallization. Fe^{3+}/Fe^{2+} ratios from orthopyroxene crystals and Fe^{3+} in plagioclase provide evidence for a relatively reduced melt that subsequently ascended, degassed and became more oxidized as a consequence of degassing. The geophysical and petrological observations suggest that dacite magma is being intruded into the Altiplano-Puna regional crustal magma body at 17 km or more depth, consistent with deformation models. In the Late Pleistocene dacitic and andesitic magmas ascended from the regional crustal magma body to a shallow magma system at a few kilometers depth where they crystallized and mingled together. The current unrest, together with geophysical anomalies and 270 ka of

*Department of Earth Sciences, University of Bristol, Bristol, BS8 1RJ, United Kingdom
**School of Geosciences, Building 28, Monash University, Victoria 3800, Australia
***Department of Earth Sciences, University of Cambridge, Cambridge CB2 3EQ, United Kingdom
§Scottish Universities Environmental Research Centre, East Kilbride, Glasgow G75 0QF, United Kingdom
§§Servicio Nacional de Geología y Minería, Avenida Santa María 0104, Santiago, Chile
§§§Empresa Minera Unificada S.A., La Paz, Bolivia; Mayelsuco@hotmail.com
‡Institute of Geophysics, University of Alaska, P.O. Box 757500, Fairbanks, Alaska 99775, USA
‡‡Department of Earth and Atmospheric Sciences, Snee Hall, Cornell University, Ithaca, New York 14853, USA
†Corresponding author: Steve.Sparks@bristol.ac.uk

dormancy, indicate that the magmatic system is in a prolonged period of intrusion. Such circumstances might eventually lead to eruption of large volumes of intruded magma with potential for caldera formation.

INTRODUCTION

Uturuncu (22° 15′S, 67° 12′W) is a Pleistocene dacite stratovolcano located in SW Bolivia (fig. 1), SE of the town of Quetana in the central Altiplano region of the Andean Central Volcanic Zone (CVZ). The volcano has been little studied, but has attracted attention due to the discovery of a large area of deformation centered on Uturuncu from InSAR studies (Pritchard and Simons, 2002, 2004). The uplift affects an area of about 70 km in diameter with a central uplift rate of approximately 1 to 2 cm/year between 1992 and 2006, making it one of the most extensive volcano-related deformation features on Earth. As a consequence of this observation a multi-national team visited Uturuncu in 2003 to carry out a reconnaissance seismic and geological survey, and to collect samples for geochronological, petrological and geochemical studies.

This paper presents the results of this investigation. We present a reconnaissance geological map and 11 high precision $^{39}Ar/^{40}Ar$ ages of the dacite lavas. Deformation

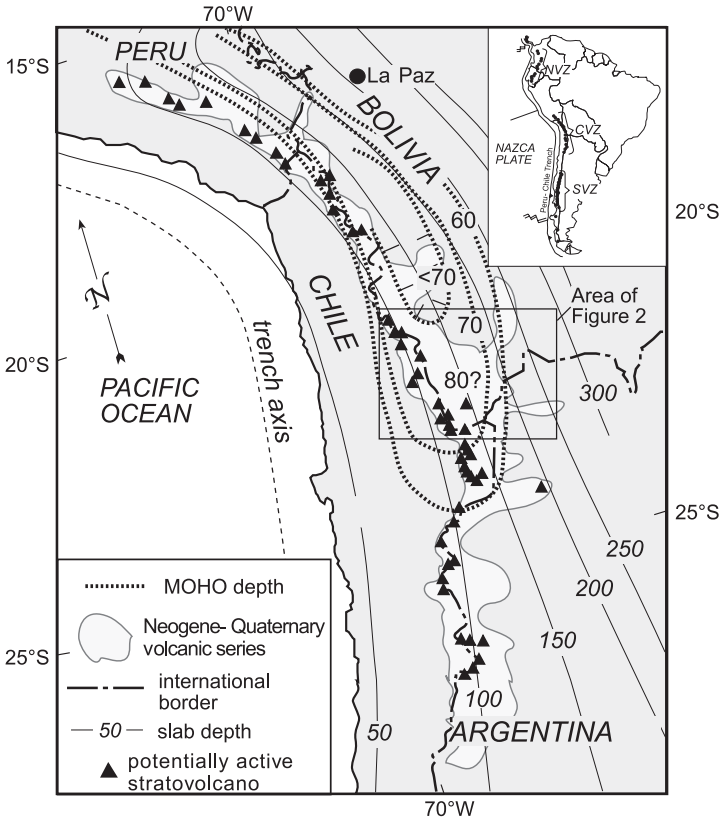

Fig. 1. Central Volcanic Zone of the Andes relative to modern depth to MOHO (Allemindinger and others, 1997) and top of slab depth in kilometers (Cahill and Isacks, 1992). Potentially active volcanoes from de Silva and Francis (1991) and Pritchard and Simons (2002). Inset shows the three active volcanic zones of the Andes: Northern (NVZ), Central (CVZ) and Southern (SVZ). Note that the moho may approach 80 km thickness in the study area as shown by the query mark. The area of figure 2 is indicated.

observations are summarized and brought up-to-date. The results of a seismic survey showing contemporary shallow seismicity are reported. The petrology and geochemistry of the lavas are described and used to constrain magma properties and magmatic conditions. This work considers the relationship of the Uturuncu system to the Altiplano-Puna regional crustal magma body, regional silicic volcanism (de Silva, 1989; Chmielowski and others, 1999; de Silva and others, 2006) and conceptual models of crustal magmatism (Annen and others, 2006, 2008; de Silva and Gosnold, 2007). The potential of Uturuncu for activity in the near future are evaluated in the context of whether the volcanic unrest is a manifestation of long-term magma intrusion or could be a sign of reawakening of a long dormant volcano.

REGIONAL BACKGROUND

The Altiplano is a broad elevated region (>3800 m) where undeformed late-Miocene and younger volcanic rocks overlie folded and faulted mid-Miocene and older volcanic and sedimentary rocks (fig. 2). Cerro Uturuncu has been constructed upon this basement during the Pleistocene. Uturuncu is located ~100 km east of the main Andean Volcanic front above an ~70 km thick crust (fig. 1; Allmendinger and others, 1997; Schmitz and others, 1999). The late Miocene and younger volcanic centers in the southern Altiplano developed along major NW-SE structures (Coira and others, 1993; Richards and Villeneuve, 2002; de Silva and others, 2006).

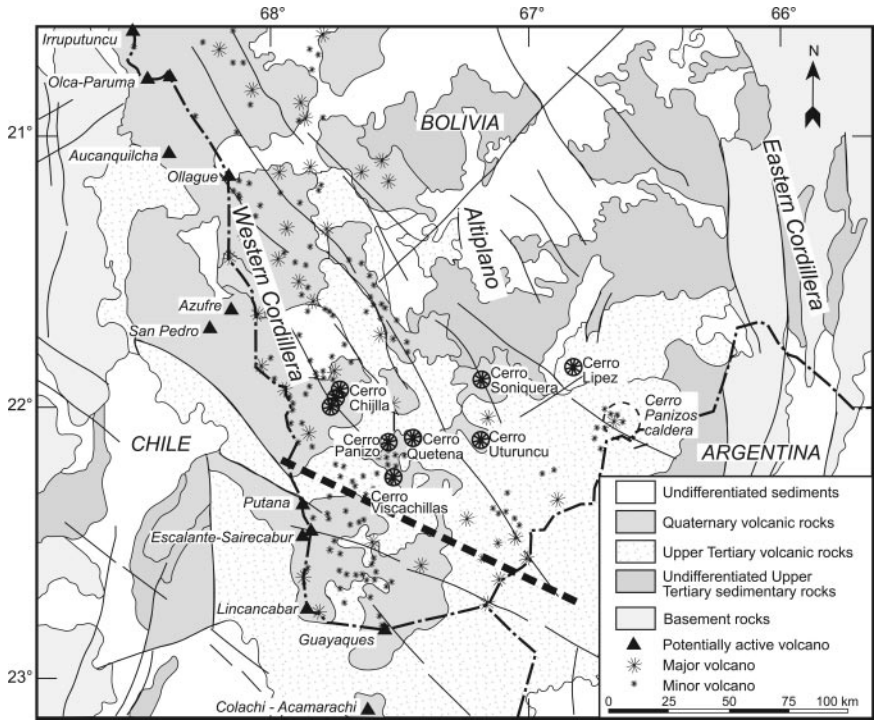

Fig. 2. Simplified geological map of southern Altiplano and surroundings (modified from Coira and others, 1993 and Marsh and others, 1992), showing location of Cerro Uturuncu. Only potentially active volcanoes (de Silva and Francis, 1991) and volcanoes on the southern Altiplano are shown. The thick dashed diagonal line trending NW-SE across the Bolivian-Argentine border (Allmendinger and others, 1997) is the boundary between the Bolivian Altiplano to the north and the Argentine Puna to the south. This boundary corresponds to lateral changes in Andean and pre-Andean paleogeography and changes in subduction zone geometry and lithosphere thickness (Allmendinger and others, 1997).

The magmatic and tectonic evolution of the central Andes is complex and is related to large-scale changes in the subduction zone configuration of the region (Stern, 2004). Modern Andean Orogeny was initiated at 26 Ma with the break-up of the Farallon plate into the Nazca and Cocos plates (Sempere and others, 1990), causing a rapid increase in the rate of convergence between the subducting oceanic plate and continental South American plate from 5 to 9 cm/yr along with an increase in the subduction angle of the oceanic slab beneath South America (Kay and others, 1999). From 26 to 12 Ma the subduction is thought to have been as a shallow flat slab in the 21 to 23°S region and the slab angle then steepened, reaching its present angle of 30° at about 3 Ma (Cahill and Isacks, 1992). The Altiplano uplift is associated with these tectonic readjustments. Uplift and thickening have been attributed to backthrusting from convergent processes (Allmendinger and others, 1997). However, the prolonged magmatism suggests that igneous intrusions must have played an important role in crustal growth and thickening.

Recent magmatism in the region (post 10 Ma) has involved voluminous ignimbrite volcanism and composite volcanoes to form the Altiplano-Puna Volcanic Complex (APVC) of de Silva (1989). The APVC covers 50,000 km^2 between 21°S and 24°S (fig. 1) and its occurrence is attributed to crustal magmatism in response to the building of the Central Andes. The APVC has been related to a large continental crustal sill-like magma body (the Altiplano Puna magma body or APMB) comprising a zone of partial melt with high electrical conductivities, low seismic velocities and low density (Schmitz and others, 1997; Schilling and others, 1997; Chmielowski and others, 1999). This zone, which extends from depths of about 17 km possibly to the base of the crust (Chmielowski and others, 1999), is interpreted as a middle to lower crustal zone of felsic and intermediate igneous composition characterized by partial melt and magma intrusions (Schmitz and others, 1997; Schilling and others, 1997). The uppermost 2 km of the APMB is a zone of very low seismic velocity (1 km/s) at 17 to 19 km (Leidig and Zandt, 2003). Pritchard and Simons (2002) found that the source of the deformation centered on Uturuncu was in excess of 17 km deep. This source depth indicates that the cause is therefore magmatic rather than hydrothermal in nature, with intrusion of new magma into the Altiplano-Puna regional crustal magma body.

CVZ lavas are amongst the most enriched in K, Rb, Th, U and other incompatible elements of any subduction-related material (Thorpe, 1984; Feeley, 1993; du Bray and others, 1995). The lavas have trace element ratios approaching the overall composition of the continental crust (Thorpe, 1984). Most of the material erupted in the CVZ is evolved andesite or dacitic-andesite. Regional dacitic ignimbrites have trace element and isotope signatures consistent with a mixed mantle and crustal origin (see de Silva and Gosnold, 2007 and references therein). The subducted oceanic crust, the overlying enriched lithospheric mantle and the lower continental crust have been proposed as possible sources for island-arc and continental margin andesites and dacites (Harmon and Hoefs, 1984; du Bray and others, 1995; de Silva and Gosnold, 2007).

METHODS

Reconnaissance Geology and Sampling

We produced a geological map based on aerial photos and 7 days of reconnaissance field-work (fig. 3), during which we were only able to visit the southern and western flanks and the summit area to collect samples. Table 1 gives locations and descriptions of the samples.

Geochronological Analytical Procedures

Fresh samples were collected from flow interiors and blocky surfaces (tables 1 and 2). Samples were screened by petrographic examination at the University of Bristol to

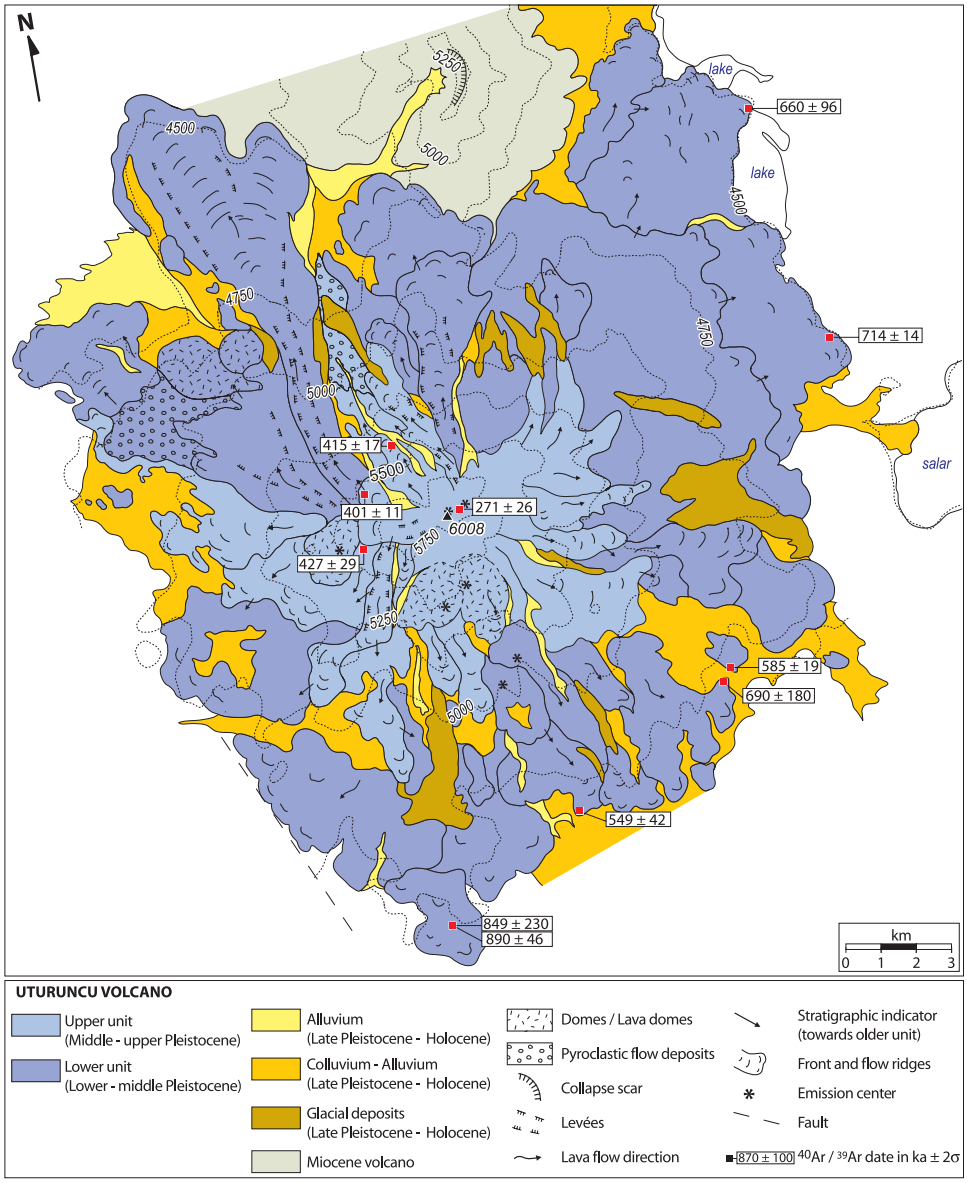

Fig. 3. Reconnaissance geological map of Uturuncu based on aerial photographs and field outcrop studies and geochronology. Locations of the new $^{39}Ar/^{40}Ar$ dates are shown.

ensure the freshest rocks were prepared for dating. Step heating analyses were performed on nine groundmass separates from dacite lavas with grain sizes of 300 to 500 μm with aliquots ranging from 300 to 475 mg. Following crushing and sieving, each sample was purified using a combination of magnetic separation, mild leaching in dilute HNO_3 and hand picking under a binocular microscope to remove phenocrysts and any altered grains. Purified separates were loaded into copper packets, placed within quartz vials and then loaded into an aluminium can for irradiation. Packets of the international standard TCR (28.34 ± 0.16 Ma, Renne and others, 1998) were

TABLE 1

Locations and description of Uturuncu samples

Sample No.	UTM Coordinates	Altitude	Sample Description
UTU 1	0680350 7541815	4385m	Porphyritic dacite block. pl-opx-ox abundant, Ox, reacted Bi and rounded qtz
UTU 2	0680350 7541815	4385m	Andesite inclusion in dacite lava abundant pl-opx-ox; qtz with cpx reaction rims
UTU 3	0680350 7541815	4385m	Devitrified pophyritic dacite lava from summit*
UTU 4	0695264 7543716	4493m	Highly vesicular dacite lava; pl- opx abundant, minor ox, qtz and bi
UTU 5	0695264 7543716	4493m	Andesite inclusion with crystal clots; fine grained with pl-bi-ox-opx
UTU 8	0696708 7538953	4516m	Porphyritic dacite lava; pl-opx-bi-ox
UTU 9	0684543 7528769	4691m	Flow-banded dacite lava; pl-opx-ox; small norite inclusions
UTU 10	0684543 7528769	4691m	Fine-grained xenoliths; qtz-rich plus bi-opx-pl.
UTU 11	0684543 7528769	4691m	Andesite inclusion. Very fine-grained, low vesicularity; pl-opx-bi
UTU 12	0684543 7528769	4691m	Coarse plutonic xenolith with pl-bi-opx-ox; radiating pl texture
UTU 13	0684543 7528769	4691m	Hornfelsed sandstone; qtz dominant with sporadic muscovite
UTU 14	0684543 7528769	4691m	Fine-grained hornfelsed sandstone; qtz dominant with sporadic muscovite and ox
UTU 15	0688313 7530540	4687m	Hand specimen - vesicular sample from older lavas. No xenoliths
UTU 16	0692102 7532853	4782m	Dacite lava; pl-opx-ox, some altered bi
UTU 17	0692102 7532853	4782m	Norite xenolith; pl-opx-cpx-bi. 120 degree triple junctions
UTU 18	0691942 7532666	4770m	Porphyritic dacite lava; pl-bi-opx-ox, minor qtz; Norite inclusions
UTU 19	0691942 7532666	4770m	Hornfelsed fine-grained igneous intrusions*
UTU 20	0690823 7532278	4830m	Highly porphyritic dacite lava with small xenoliths; pl-bi-opx-ox; rounded quartz
UTU 21	0683839 7542286	4687m	Dacite lava; pl-bi-opx-ox; rounded qtz
UTU 22	0685672 7538816	5275m	Flow banded dacite lava; pl-opx-bi-qz-ox; minor cpx and am
UTU 23	0687400 7536808	5791m	Glassy dacite lava from western summit; pl-bi
UTU 24	0687400 7536808	5791m	Fine grained equigranular andesite inclusion; pl-cpx around qtz
UTU 25	0687400 7536808	5791m	Porphyritic dacite lava with large biotite crystals; pl-bi-qtz but low opx
UTU 26	0687400 7536808	5791m	Andesite inclusion; slightly weathered; opx-pl-amp-bi.
UTU 27	0687400 7536808	5791m	Several andesite inclusions opx-pl-amp-bi.with acicular amp
UTU 28	0686569 7537484	5689m	Glassy dacite lava from eastern vent with rounded bi; pl-opx-bi-ox-qtz
UTU 29	0686569 7537484	5689m	Fine-grained andesite inclusion; pl-opx-amp-cpx
UTU 30	0686569 7537484	5689m	Fine-grained andesite inclusion; pl-opx-amp-cpx-bi
UTU 31	0685778 7536964	5570m	Glassy dacite lava; pl-opx-bi-ox
UTU 32	0685778 7536964	5570m	Three metamorphic inclusions; sillimanite, cordierite and alkali feldspar
UTU 33	0685263 7536528	5479m	Dacite lava with andesite and norite inclusions; pl-opx-bi
UTU 34	0685263 7536528	5479m	Andesite inclusion; opx dominant with pl and qtz
UTU 35	0685263 7536528	5479m	Orbicular norite xenolith; radial layers of opx-pl-bi
UTU 36	0685263 7536528	5479m	Microgranular inclusion; qtz with some cpx and bi and isolated biotite
UTU 37	0685115 7536621	5530m	Dacite lava; pl-bi-opx-ox; rounded qtz, also am-cpx inclusion
UTU 38	0685115 7536621	5530m	Dacite lava; pl-opx-bi-ox, rounded qtz
UTU 39	0685115 7536621	5530m	Fine-grained dacite lava; pl-opx-cpx
UTU 40	0685115 7536621	5530m	Andesite inclusion*

Mineralogy based in thin sections. pl = plagioclase; opx = orthopyroxene; cpx = clinopyroxene; bi = biotite; ox = oxide; qtz = quartz; amp = amphibole; * no thin section.

interspersed with the Cu sample packets to permit characterization of the irradiation flux to the samples; J values assume ± 0.5% (1σ) precision. The samples were irradiated in the Petten HFR reactor for 1 hour, in the Cd-lined facility (RODEO).

Samples were step heated using a resistively heated double-vacuum furnace over a range of temperatures from 500 to 1600°C, with the number of steps ranging from 11 to 31 per experiment. Furnace blanks were stable at less than 1.2×10^{-14} mol ^{40}Ar, 8.5×10^{-17} mol ^{39}Ar, 6.8×10^{-17} mol ^{38}Ar, 6.8×10^{-17} mol ^{37}Ar and 1.4×10^{-16} mol ^{36}Ar. Sample to blank ratios ranged from 20 to 1300 (^{40}Ar), 40 to 40,000 (^{39}Ar) and 8 to 900 (^{36}Ar) for selected plateau steps. Data were collected at SUERC (East Kilbride) on an Argus multi-collector mass spectrometer (Alexandre and others, 2006). The Argus employs five high-gain, low-noise Faraday cups with 10^{11} (^{40}Ar) and 10^{12} ($^{39\text{-}36}$Ar) ohm resistors for simultaneous collection of all five isotopes of argon. Peak intensities are regressed to sample inlet time using second-order polynomial regressions. All ratios are blank and mass discrimination corrected. Ratios used for inverse isochron calculations are corrected for irradiation-induced interferences. The geochronological results are

TABLE 2

Geochronological data on Uturuncu dacite lava samples

Sample	Mass (g)	J x 10^4	Fusion age (ka)	2σ	%40atm (total)	K/Ca	2σ	Plateau steps °C	Plateau Isochron (ka)
UTU4A	320	3.333	647	7	56	5.4	0.2	800-1050	660
UTU8	333	3.337	742	7	72	12.2	0.5	750-1250	714
UTU9	329	3.334	696	7	92	41.7	1.6	500-800	849
UTU11	400	3.295	954	10	61	10.8	0.4	950-1050	890
UTU15	328	3.311	609	6	95	10.5	0.4	750-1150	549
UTU16	323	3.314	611	6	39	13.3	0.5	850-1000	585
UTU18	334	3.312	868	9	92	8.0	0.3	800-1000	690
UTU25	300	3.338	283	3	69	15.1	0.6	850-1100	271
UTU28	346	3.290	405	4	57	37.8	1.5	950-1100	415
UTU31	360	3.329	421	4	42	28.5	1.1	900-1250	401
UTU33	475	3.321	407	4	89	38.2	1.5	900-1450	427

Sample	2σ	% ^{39}Ar	^{40}Ar/^{36}Ar(i)	2σ	MSWD	N	Fit
UTU4A	96	79	336	36	1.2	10 of 19	0.31
UTU8	14	100	301.8	2.6	1.1	12 of 14	0.38
UTU9*	230	100	290.9	6.8	0.24	11 of 11	0.99
UTU11	46	63	334	21	1.2	8 of 26	0.29
UTU15	42	98	295.4	1.6	0.52	19 of 31	0.95
UTU16	19	84	325	14	0.64	7 of 14	0.67
UTU18	180	90	303	13	0.77	8 of 18	0.59
UTU25	26	59	286	11	0.11	6 of 14	0.98
UTU28	17	88	294	14	0.13	6 of 14	0.97
UTU31	11	86	308	13	1.3	9 of 16	0.22
UTU33	29	99	292.1	3.2	0.28	19 of 25	1.00

J values are calculated relative to TCR2a standard (TCR − 28.34 ± 0.16 Ma, Renne and others, 1998). Estimated error on J is 0.5%. Ages calculated with lamda of 5.543×10^{-10}/year. Data are corrected for ^{37}Ar and ^{39}Ar decay, half-lives of 35 and 259 years respectively. * denotes large step loss. Locations of samples are in table 1.

given in table 2 with details in Supplementary Data Table I http://earth.geology.yale.edu/~ajs/SupplementaryData/2008/01SparksTableI.xls.

Petrological and Geochemical Analytical Techniques

36 samples were investigated, comprising 20 dacitic lava samples, 8 andesite inclusions and 8 xenoliths. The Bolivia Geological Service also performed XRF analyses of 18 lava samples as reported in Mayel Sunagua (2002). These results are included in this study.

Thin sections of 36 samples were inspected and modal proportions analyzed (table 3) with approximately 1500 points counted per sample, in rows of 500 points, 4 mm apart. X-ray fluorescence (XRF) analyses of major and trace elements were performed at Leicester University using standard techniques described by Harvey and others (1996). Analyses of international reference materials indicate that accuracy and precision are better than 0.5 percent for major elements and better than 3 percent for trace elements. XRF data are presented in tables 4A and 4B. Electron probe microanalysis (EPMA) of minerals was performed at the University of Bristol on a JEOL JXA-8600 four-spectrometer instrument with LINK analytical X-ray analysis system and LEMAS

TABLE 3

Modal analyses

Sample Type	UTU1 Lava	**UTU2 Incn**	**UTU4 Lava**	UTU5 Incn	UTU8 Lava	UTU9 Lava	**UTU10 Xeno**	UTU11 Lava	**UTU12 Xeno**	UTU13 Xeno	UTU14 Xeno	UTU15 Lava	UTU16 Lava	**UTU17 Xeno**	**UTU18 Lava**	UTU20 Lava	**UTU21 Lava**	**UTU22 Lava**
Plag Phenocrysts	9.08	**7.51**	**6.9**	8.75	9.85	10.98	**1.3**	8.39	**32.4**	1.4	-	9.4	10.84	**43.9**	**14.2**	11.91	**9.87**	**11.3**
Plag Microphenocrysts	9.27	**16.48**	**9.06**	27.01	14.23	14.46	**27.1**	11.54	**11.5**	29.6	0.88	10.14	12.77	**11.1**	**6.88**	8.71	**6.79**	**8.64**
Opx Phenocrysts	4.14	**3.82**	**2.76**	6.38	2.8	6.17	**1.9**	6.08	**25.6**	-	-	6.66	6.36	**28.2**	**6.16**	8.02	**2.07**	**3.6**
Opx Microphenocrysts	7.56	**8.55**	**7.74**	10.12	5.16	9.21	**13.1**	7.57	**12.1**	-	8.63	7.4	8.77	**10.1**	**6.16**	7.17	**4.2**	**8.46**
Quartz Phenocrysts	1.18	**1.45**	**0.75**	0.77	0.39	0.44	**22.3**	1.13	**5.1**	37.2	12.03	0.33	0.43	**-**	**1.24**	0.49	**3.33**	**0.77**
Quartz Microphenocrysts	-	**-**	**-**	-	-	-	**28.7**	-	**2**	22.8	29.04	-	-	**-**	**-**	-	**-**	**-**
Cpx Phenocrysts	0.72	**0.21**	**-**	-	-	-	**-**	-	**-**	-	-	-	-	**4.1**	**-**	-	**-**	**-**
Cpx Microphenocrysts	-	**1.66**	**-**	-	-	-	**-**	-	**-**	8.9	4.28	-	-	**0.3**	**-**	-	**-**	**-**
Oxides	1.98	**1.08**	**1.65**	0.66	3.7	5.05	**2.5**	1.79	**2**	2.1	7.88	2.92	3.23	**0.7**	**2.6**	2.59	**1.96**	**3.92**
Biotite Phenocrysts	4.45	**0.54**	**0.96**	1.32	6.71	2.5	**3.1**	2.34	**15**	-	-	-	0.47	**1.6**	**2.64**	1.46	**6.69**	**5.99**
Amphibole Phenocrysts	-	**-**	**-**	-	-	-	**-**	-	**-**	-	-	-	-	**-**	**-**	-	**-**	**0.95**
Total Crystals %	38	**41.5**	**30**	55	43	49	**100**	39	**100**	100	63	37	43	**100**	**40**	40.5	**35**	**45**
Total Groundmass %	62	**58.5**	**70**	45	57	51	**0**	61	**0**	0	37	63	57	**0**	**60**	59.5	**65**	**55**

Sample Type	UTU23 Lava	UTU24 Incn	**UTU25 Lava**	UTU26 Incn	UTU27 Incn	**UTU28 Lava**	UTU29 Incn	UTU30 Lava	UTU30 Incn	UTU31 Lava	UTU33 Lava	UTU34 Incn	**UTU35 Xeno**	UTU36 Xeno	UTU37 Lava	**UTU38 Lava**	UTU38 Xeno	UTU39 Lava
Plag Phenocrysts	8.65	10.2	**10.66**	15.68	15.19	**9.91**	17.26	6.81	19.62	10.17	12.52	10.21	**30.7**	1.87	11.75	**10.44**	15.8	7.76
Plag Microphenocrysts	9.8	21.06	**10.94**	13.05	17	**8.27**	11.23	7.08	18.23	12.65	14.28	13.93	**14.5**	-	13.05	**12.84**	22.1	13.48
Opx Phenocrysts	6.99	7.84	**1.39**	8.03	9.31	**3.61**	11.1	4.29	8.01	6.44	8.51	8.49	**38.6**	3.15	10.62	**2.28**	-	6.4
Opx Microphenocrysts	7.15	14.1	**4.42**	5.14	7.75	**8.74**	10.75	4.16	11.83	8.01	10.27	11.04	**12.4**	7.98	10.51	**4.4**	-	12.17
Quartz Phenocrysts	1.11	0.18	**5.76**	0.535	0.5	**3.15**	0.21	0.64	0.15	2.57	1.87	3	**-**	43.04	1.92	**1.08**	62	0.19
Quartz Microphenocrysts	-	-	**-**	-	-	**-**	-	-	-	-	-	-	**-**	29.35	-	**-**	-	-
Cpx Phenocrysts	-	-	**-**	2.35	1.94	**-**	-	-	-	0.14	0.11	-	**-**	-	-	**-**	-	2.28
Cpx Microphenocrysts	-	-	**-**	1.02	1.44	**-**	5.14	-	5.07	-	-	-	**-**	8.77	-	**-**	-	1.5
Oxides	3.52	4.8	**4.75**	4.23	5.75	**2.73**	10.89	2.07	9.85	1.67	2.78	3.83	**0.5**	1.18	3.11	**0.8**	-	4.51
Biotite Phenocrysts	2.21	0.12	**10.03**	2.46	2.44	**5.42**	0.411	1.38	0.29	3.15	3.16	4.77	**3**	3.15	5.54	**8.04**	-	-
Amphibole Phenocrysts	-	-	**-**	0.803	1.19	**-**	-	-	0.441	-	-	-	**-**	-	-	**-**	-	-
Total Crystals %	39.5	58.5	**48**	53.5	62.5	**42**	68.5	26.5	73.5	45	53.5	55.5	**100**	98.5	56.5	**40**	100	48.5
Total Groundmass %	60.5	41.5	**52**	46.5	37.5	**58**	31.5	63.5	26.5	55	46.5	44.5	**0**	1.5	43.5	**60**	0	51.5

i) Point count analyses undertaken using Nikon optical microscopes, ii) Samples in bold type were further analyzed using SEM and electron microprobe

Table 4A

XRF analyses of lavas

Sample	UTU 1	UTU4	UTU8	UTU9	UTU11	UTU15	UTU16	UTU18	UTU20	UTU21	UTU22	UTU23	UTU25	UTU28	UTU31	UTU33	UTU37	UTU38
Type	Lava	Lava	Lava	Lava	Lava	Lava	Lava	Lava	Lava	Lava	Lava	Lava	Lava	Lava	Lava	Lava	Lava	Lava
SiO_2	63.02	62.33	63.16	65.12	65.69	64.32	64.93	63.41	64.79	65.64	64.43	66.80	65.25	63.76	63.23	64.04	64.43	62.33
TiO_2	1.03	1.11	1.12	1.24	1.22	1.11	1.24	1.31	1.25	1.16	1.33	1.14	1.18	1.19	1.17	1.11	1.20	1.16
Al_2O_3	16.20	16.75	16.63	16.07	15.74	16.51	16.31	16.62	16.42	16.50	16.41	15.79	16.24	16.16	16.21	16.19	16.38	16.06
Fe_2O_3	5.81	6.28	5.88	5.20	5.28	5.58	5.66	6.03	5.46	4.67	5.26	4.61	4.80	5.52	5.79	5.43	5.33	6.25
MnO	0.07	0.08	0.07	0.06	0.05	0.06	0.07	0.07	0.07	0.06	0.06	0.05	0.06	0.07	0.07	0.08	0.07	0.09
MgO	2.54	2.65	2.29	1.87	1.80	1.85	1.96	2.40	1.94	1.55	2.13	1.57	2.13	2.67	3.09	2.86	2.29	3.76
CaO	5.17	4.87	4.61	4.15	4.01	4.22	3.90	4.38	3.86	3.58	3.98	3.32	3.74	4.44	4.30	4.24	4.39	5.15
Na_2O	2.31	2.25	2.23	2.22	2.26	2.43	2.36	2.17	2.32	2.35	2.23	2.34	2.38	2.26	2.28	2.24	2.00	2.10
K_2O	3.56	3.39	3.73	3.75	3.58	3.62	3.26	3.29	3.59	4.18	3.82	4.07	3.92	3.61	3.54	3.51	3.61	2.82
P_2O_5	0.27	0.28	0.29	0.31	0.30	0.29	0.31	0.30	0.30	0.32	0.35	0.31	0.30	0.31	0.31	0.30	0.30	0.29
SO_3	0.019	0.012	0.012	0.010	0.059	0.007	-0.002	0.001	0.001	0.000	0.012	0.001	0.012	0.005	0.006	0.006	0.000	0.001
Total	100.00	100.00	100.00	100.00	100.00	100.00	100.00	100.00	100.00	100.00	100.00	100.00	100.00	100.00	100.00	100.00	100.00	100.00
LOI	1.16	1.19	0.86	1.14	0.59	1.51	0.97	1.13	0.77	1.41	0.34	1.67	1.26	1.24	1.57	1.15	2.16	0.67
Mo	1.3	1.8	1.6	0.9	1.0	1.3	1.3	1.8	1.1	1.7	1.9	1.8	1.3	1.6	1.7	1.4	1.5	1.5
Nb	17.8	20.2	20.4	23.8	22.1	18.1	19.6	21.0	19.7	22.4	22.1	20.5	27.0	20.6	20.3	21.1	21.0	19.9
Sr	405	423	406	386	382	356	349	382	360	391	385	430	474	427	406	415	401	440
Rb	155	152	169	170	163	175	187	153	177	202	216	178	203	179	173	176	184	151
Zr	239	242	243	271	258	274	282	245	272	261	256	272	265	248	246	250	241	231
Y	29.1	33.2	30.8	26.7	23.5	26.7	24.7	25.6	23.4	21.9	20.5	23.5	20.3	25.8	25.0	24.7	24.7	27.2
U	3.8	4.7	3.7	2.5	1.7	3.9	2.6	3.0	3.5	5.0	5.1	4.6	3.7	4.1	4.5	3.9	1.9	2.2
Th	22.4	20.6	22.2	25.3	26.4	29.5	27.7	24.7	27.9	27.8	28.9	26.4	25.9	24.8	24.4	25.3	22.1	20.6
Pb	21.1	19.4	20.5	23.1	18.5	21.3	22.5	19.7	25.8	27.6	26.2	21.2	25.4	20.9	20.8	20.7	21.9	16.1
Ga	21.7	22.3	23.6	23.2	22.2	22.1	22.4	22.8	22.6	23.6	23.6	22.6	23.7	22.3	21.8	22.3	22.2	21.0
Zn	90.1	89.8	93.6	96.3	96.2	94.1	95.1	89.5	98.6	101.1	97.9	101.3	95.7	98.4	92.8	93.5	91.4	92.5
Cu	4.5	5.4	6.2	8.2	8.1	5.2	10.7	5.7	7.2	4.8	6.8	6.6	3.1	6.2	13.1	5.4	5.0	7.2
Ni	4.4	2.4	1.7	3.7	5.2	1.9	4.1	4.4	5.5	2.8	6.2	4.6	3.2	6.0	0.4	2.9	2.0	2.2
Co	14.9	14.9	12.7	12.1	10.7	11.7	12.9	13.2	12.1	9.5	11.7	12.5	11.7	12.9	12.4	13.4	13.2	16.1
Sc	17.8	16.8	13.7	11.1	10.6	12.6	10.8	10.3	11.2	9.3	8.6	11.0	12.5	12.8	15.2	14.5	12.5	21.1
Ba	734	762	843	818	837	798	774	806	821	961	918	893	960	825	786	815	862	766
V	127	130	119	104	116	110	116	120	111	91	90	113	105	121	115	121	121	129
Cr	1.5	0.2	7.7	4.9	10.4	8.9	7.2	4.5	7.7	11.2	9.0	7.2	1.2	9.9	51.6	30.8	0.8	74.5
La	47.8	50.6	50.3	58.0	51.7	59.8	63.2	55.3	58.5	61.8	62.0	60.7	57.3	57.4	52.8	55.4	55.7	49.0
Nd	46.4	47.2	47.5	53.2	52.2	56.6	60.0	49.0	57.1	59.3	56.0	55.0	52.0	52.7	47.1	53.7	49.5	44.7
Cs	9.1	8.0	0.5	2.4	6.9	6.6	1.3	6.8	1.7	11.4	12.1	1.1	2.9	8.9	6.3	7.6	9.8	2.8

TABLE 4B

XRF analyses of andesite inclusions and xenoliths

Sample Type	UTU2 Andesite inclusion	UTU5 Andesite inclusion	UTU26 Andesite inclusion	UTU27 Andesite inclusion	UTU30 Andesite inclusion	UTU34 Andesite inclusion	UTU39 Andesite inclusion	UTU10 Qtz-rich xenolith	UTU12 Norite xenolith	UTU17 Norite xenolith	UTU32 Gneiss xenolith
SiO_2	60.75	59.62	58.94	59.12	57.62	61.20	57.27	74.05	54.36	50.84	58.93
TiO_2	1.06	1.17	1.51	1.60	1.46	1.34	1.43	0.58	0.49	1.32	1.03
Al_2O_3	16.77	17.19	17.14	17.75	17.48	16.08	17.58	10.01	22.05	16.96	22.89
Fe_2O_3	6.70	7.11	6.11	5.73	7.40	6.50	7.54	6.45	6.55	10.56	6.10
MnO	0.10	0.11	0.09	0.09	0.10	0.09	0.10	0.12	0.10	0.14	0.09
MgO	3.13	3.37	4.43	3.64	4.71	4.69	5.38	2.87	4.95	10.22	1.67
CaO	6.16	5.81	6.31	5.94	6.65	4.68	7.28	4.92	8.72	8.59	5.04
Na_2O	2.26	2.16	2.22	2.57	1.90	1.87	1.72	0.50	1.81	0.98	1.31
K_2O	2.72	2.98	2.72	3.17	2.36	3.20	1.42	0.34	0.88	0.20	2.79
P_2O_5	0.26	0.29	0.49	0.36	0.28	0.31	0.28	0.13	0.08	0.18	0.16
SO_3	0.100	0.215	0.032	0.046	0.029	0.042	-0.001	0.022	0.007	0.007	0.009
Total	100.00	100.00	100.00	100.00	100.00	100.00	100.00	100.00	100.00	100.00	100.00
LOI	1.88	1.92	1.88	2.46	1.68	2.66	-0.05	0.30	1.09	0.34	2.36
Mo	1.1	1.4	2.1	2.6	1.6	1.4	0.6	0.5	0.6	0.6	0.9
Nb	16.2	20.1	36.1	40.8	19.0	20.4	16.8	11.2	8.0	9.9	18.9
Sr	430	470	790	867	523	412	524	182	538	551	387
Rb	111	120	127	131	92	137	83	18	43	7	82
Zr	213	242	239	261	207	220	179	254	66	107	186
Y	34.2	41.5	29.9	28.0	26.3	27.2	25.8	39.9	10.2	18.3	38.6
U	1.4	3.6	1.9	2.4	2.0	2.3	1.4	1.8	0.7	0.6	2.9
Th	17.6	19.0	25.8	23.9	14.0	20.2	12.8	17.2	10.6	4.8	22.4
Pb	16.6	17.5	17.8	15.9	10.2	17.3	10.4	2.6	11.7	5.3	27.0
Ga	20.5	21.2	22.9	22.9	22.0	22.0	22.4	14.0	26.8	21.5	30.4
Zn	84.4	97.3	95.2	81.1	90.8	122.5	83.8	89.2	120.3	125.6	125.3
Cu	5.8	7.0	7.6	10.2	8.8	6.8	7.1	27.3	10.0	21.2	80.4
Ni	2.2	5.2	8.6	3.0	4.9	3.7	1.3	14.4	9.0	10.2	9.6
Co	16.9	18.7	15.8	13.8	19.2	17.6	19.6	15.7	20.0	36.5	14.6
Sc	23.1	21.7	20.1	19.3	21.1	19.6	19.6	14.0	18.1	33.7	16.6
Ba	732	734	995	1152	656	756	658	202	379	197	626
V	149	159	158	151	167	167	173	52	182	252	136
Cr	7.3	1.6	39.7	1.3	32.1	78.8	50.3	19.3	61.8	338.3	63.9
La	40.2	45.3	78.6	87.2	40.1	48.0	48.7	35.0	20.1	19.7	49.9
Nd	41.3	43.7	62.7	57.8	36.8	45.7	44.1	31.8	18.9	19.0	43.2
Cs	6.8	6.4	1.7	4.1	4.9	3.8	3.0	3.2	-0.6	1.7	2.6

TABLE 4C

Matrix glass compositions from Uturuncu lavas

Sample Type	UTU 2 Andesite inclusion	UTU 25 Lava	UTU 28 Lava	UTU 4 Lava	UTU 38 Lava	UTU 18 Lava
SiO_2	77.70	79.20	78.72	77.71	79.13	75.85
TiO_2	0.49	0.20	0.37	0.46	0.56	0.32
Al_2O_3	11.57	11.73	11.45	11.75	11.69	13.17
FeO_T	1.42	0.87	1.01	1.22	0.60	0.35
MnO	0.10	0.07	0.03	0.04	0.00	0.03
MgO	0.11	0.00	0.06	0.13	0.02	0.06
CaO	0.53	0.44	0.50	0.42	0.41	0.66
Na_2O	1.54	1.45	1.72	1.58	1.16	2.23
K_2O	6.11	5.91	5.83	5.96	5.93	6.76
Total	99.56	99.88	99.72	99.26	99.53	99.45

automation. Representative mineral analyses are in Supplementary Table II http://earth.geology.yale.edu/~ajs/SupplementaryData/2008/02SparksTableII.xls.

Glasses and melt inclusions in plagioclase, orthopyroxene, biotite and apatite, were analyzed using a CAMECA SX-100 five-spectrometer instrument. Data are presented in tables 4C and 4D. Run conditions were 20 kV accelerating voltage, beam current of 15 nA and a 5 μm beam diameter for mineral traverses. Melt inclusions were analyzed in plagioclase using the protocol described in Humphreys and others (2006a). Water contents of hydrous melt inclusions were estimated using the by-difference method, with H as a difference element in an oxygen stoichiometric PAP correction model. Errors on H_2O are approximately ±0.6 weight percent (Devine and others, 1995; Humphreys and others, 2006a).

GEOLOGY

Cerro Uturuncu is a stratovolcano, with a summit elevation of 6008 m above sea level (fig. 4A). It is the highest peak of SW Bolivia, and covers an area of about 400 km^2. We estimate an approximate extant volume of 85 km^3 assuming a base level of 4500 m. The volcano is composed principally of dacite lavas and domes. Much of the volcano has been smoothed by glacial activity (fig. 4B), and no large collapse scars have been identified. The volcanic products have been divided, on the basis of distribution and age data, into a Lower to Middle Pleistocene lava sequence (fig. 3), with lavas extending to distances of up to 15 km, and an Upper to Middle Pleistocene sequence of lavas and domes that extend up to 10 km and form the upper parts of the edifice (fig. 3). Although lava flows display well preserved flow features, the youngest summit lavas have been glaciated (fig. 4). Two active sulfur-producing fumarole fields are located near the summit. We measured temperatures in the fumaroles of slightly below 80°C in May 2003.

The lavas are blocky, flow-banded, glassy and porphyritic with steep, broken-up flow fronts of tens of meters thickness (fig. 4C). Most of the lavas contain andesite inclusions, making up no more than a few percent of the lava. Many lavas also contain norite inclusions, many of which contain minor biotite. We found an orbicular norite inclusion with concentric layering around an homogeneous core. Xenoliths in the dacite lavas include quartz-rich igneous rocks and sillimanite gneiss.

TABLE 4D

Analyses of glass inclusions in minerals to estimate the water content by difference, using method of Humphreys and others (2006)

Sample	UTU2	UTU2	UTU2	UTU4	UTU4	UTU17	UTU17	UTU18	UTU21	UTU21	UTU21	UTU21	UTU21	UTU21	UTU22	UTU25	UTU25	UTU25	UTU38
Host	Plag	Plag	Opx	Opx	Opx	Plag	Plag	Bt	Bt	Bt	Plag	Apt	Opx	Plag	Bt	Opx	Bt	Bt	Bt
SiO_2	71.54	70.76	69.70	73.17	73.76	69.74	77.38	71.30	72.79	73.07	73.53	68.52	71.05	75.09	73.50	68.32	68.49	72.71	72.90
TiO_2	0.34	0.16	0.17	0.15	0.35	0.16	0.55	0.59	0.18	0.21	0.24	0.12	0.32	0.19	0.51	0.14	0.06	0.25	0.58
Al_2O_3	13.57	13.39	13.48	12.29	12.31	16.96	10.42	13.36	13.19	11.89	12.51	12.55	12.33	11.51	12.81	15.83	15.53	13.06	12.90
FeO_T	1.54	1.07	1.44	2.35	1.24	0.47	0.57	1.15	1.48	1.33	1.60	4.30	2.01	1.56	1.13	1.20	1.46	0.69	1.16
MnO	0.00	0.01	0.03	0.05	0.03	0.00	0.00	0.00	0.05	0.05	0.02	0.17	0.00	0.00	0.02	0.00	0.01	0.02	0.02
MgO	0.16	0.10	0.17	0.18	0.05	0.09	0.10	0.13	0.16	0.21	0.28	0.66	0.26	0.17	0.03	0.03	0.16	0.08	0.09
CaO	2.09	1.37	1.85	1.03	0.69	4.74	0.37	0.44	0.69	0.48	0.52	5.05	1.24	0.41	0.30	0.51	0.40	0.48	0.59
Na_2O	2.35	2.47	2.95	2.26	2.12	1.86	1.62	2.42	2.12	1.81	1.94	2.08	2.39	1.83	2.14	3.54	3.50	2.48	2.36
K_2O	5.86	5.08	6.78	5.06	6.20	4.25	5.63	6.85	6.18	6.10	6.11	4.89	5.83	5.96	6.24	7.44	6.77	6.00	6.93
P_2O_5	0.03	0.09	0.02	0.20	0.19	0.03	0.06	0.16	0.15	0.08	0.06	0.09	0.11	0.01	0.12	0.20	0.05	0.07	0.05
F	0.10	0.05	0.13	0.19	0.11	0.08	0.07	0.10	0.09	0.08	0.09	0.04	0.07	0.10	0.33	0.09	0.04	0.09	0.14
SO_2	0.03	0.00	0.08	0.02	0.00	0.02	0.00	0.00	0.02	0.00	0.00	0.00	0.00	0.00	0.01	0.00	0.01	0.00	0.00
Cl	0.13	0.14	0.10	0.13	0.16	0.10	0.11	0.17	0.14	0.10	0.18	0.07	0.13	0.15	0.11	0.24	0.32	0.10	0.15
H_2O	**2.25**	**5.32**	**3.09**	**2.93**	**2.78**	**1.47**	**3.11**	**3.30**	**2.77**	**4.58**	**2.92**	**1.43**	**4.26**	**2.97**	**2.75**	**2.44**	**3.20**	**3.98**	**2.13**
Total	97.74	94.69	96.90	97.08	97.21	98.50	96.88	96.67	97.24	95.41	97.08	98.54	95.74	96.98	97.25	97.54	96.80	96.03	97.87

Notes;
i) Oxides, elemental abundances, and water contents calculated using a CAMECA Electron Microprobe
ii) Abbreviations: Plag – plagioclase, Opx – orthopyroxene, Bt - biotite, Apt - apatite
iii) All samples are dacite lavas except for UTU 2 - andesite inclusion and UTU 17 - norite xenolith

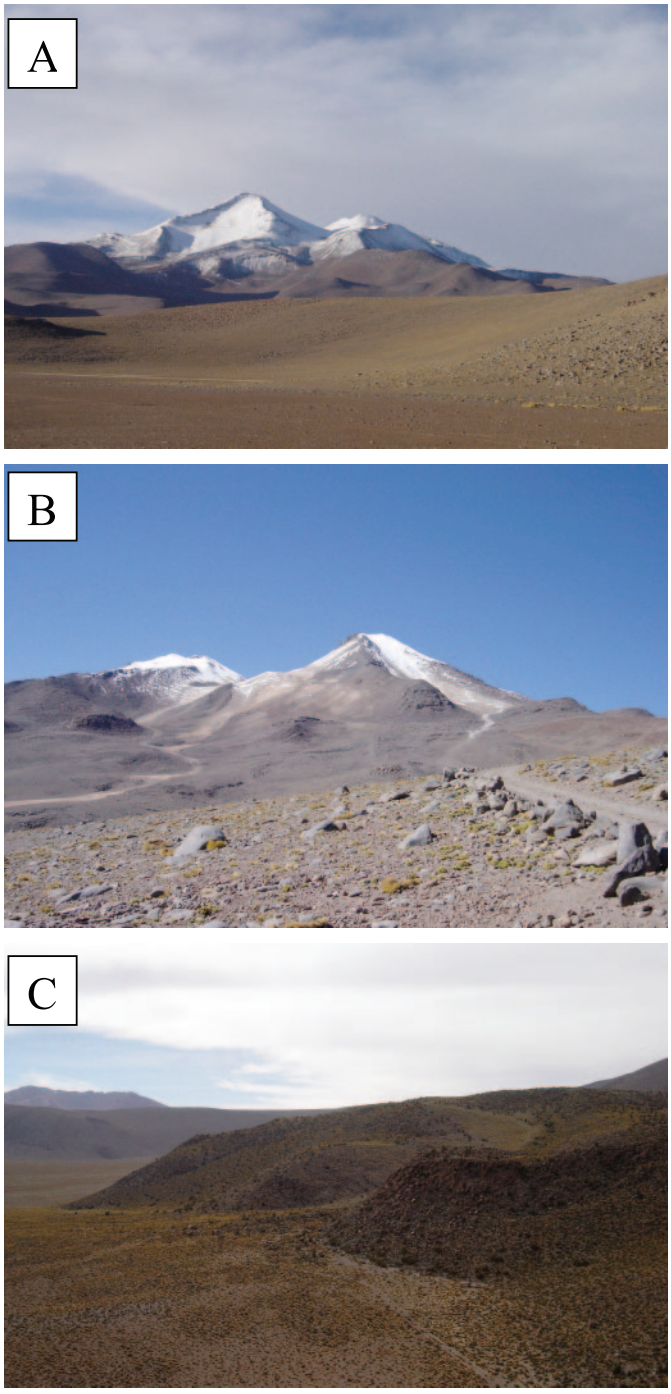

Fig. 4. (A) View of Uturuncu from 15 km to the east. The summit lava has an age of 271 ka. (B) View of the summit region from 5 km to the east. The terrain is smoothed by glaciation and the outcrops of the dacite lavas show prominent flow banding. (C) Flow fronts of the oldest lavas at the base of the volcano on the southern flanks. These lavas have an age of 549 ka.

GEOCHRONOLOGY

Table 2 summarizes the geochronologic data and gives results for total fusion ages and 'plateau-chron' ages in ka. The plateau-chron calculations are derived from the Isoplot 3.0 software (Ludwig, 2003); this method constructs both an inverse isochron (fig. 5) and a plateau calculation that is internally consistent and accounts for the variability and uncertainty in the trapped component. Plateau acceptance criteria are N = 3 for minimum number of contiguous steps, F = 0.60 (that is, ≥60% of ^{39}Ar released) and P = 0.05 for the probability of fit. Four samples (UTU 4a, 8, 11 and 16) show the presence of excess argon at the 2σ level, that is, trapped component > 295.5 ± 0.5. The plateau-chron ages are concordant with total fusion ages within 2σ limits, and we accept the plateau-chron ages as the best estimates of timing of eruption. Air contamination of samples was variable, ranging from 39 to 95 percent atmospheric ^{40}Ar. Age uncertainties account for analytical errors and estimated uncertainty in J (±0.5%).

A previous study by the Geological Survey of Bolivia proposed an age <1 Ma around the summit with older flows to the North and West (10–15 Ma) (Carta Geologica De Bolivia, 1996). The new data confirm the age limit as less than 1 Ma but indicate that the volcano is made of an older sequence of lava flows (890 – 549 ka) and a younger sequence of less extensive lava flows (427–271 ka). The morphologically youngest summit lava dome has an age of 271 ka, showing that the volcano is long dormant. Kussmaul and others (1977) suggested that there were postglacial lavas, but de Silva and Francis (1991) reported from inspection of satellite images that there was no evidence for postglacial activity, a conclusion that is now confirmed.

DEFORMATION

Observations

We made a total of 17 interferograms for Uturuncu spanning 14.5 years (5/2/1992 to11/20/2006) from the ERS-1, ERS-2, and Envisat satellites of the European Space Agency, with five new interferograms adding six years of data to the prior work of Pritchard and Simons (2002, 2004). Almost all of the interferograms have the same viewing geometry (ERS-1/2 descending orbits or Envisat Beam 2 descending orbit). However, data from two ascending orbits, two different Envisat beams, and two separate ERS descending orbits allow us to recover more than one component of deformation. Uturuncu is the only central Andean volcano observed to be deforming during the entire 14 years of InSAR observations, although the rate of deformation is variable (figs. 6 and 7) between 1 to 2 cm/yr in the radar line-of-sight (LOS) direction.

Deformation Models

Observations of surface deformation provide non-unique constraints on the depth and volume change of magma (for example, Dieterich and Decker, 1975). Therefore, we explored a variety of different elastic models that fit the data to estimate a range of plausible source characteristics (Pritchard and Simons, 2004), including: penny-shaped cracks (sills) as point or finite sources (Fialko and others, 2001), prolate ellipsoid point sources with variable dips (Yang and others, 1988), and spherical point sources in a homogeneous or layered elastic half-space. For each type of source, we use several non-linear inversion methods to find the model parameters that best match the data in a least-squares sense. Given the limited InSAR data available, all types of data can fit the data within the level of noise, with the different shaped deformation sources at different depths (for example, Dieterich and Decker, 1975). For further details on the inversion methodology and a detailed discussion of the results, see Pritchard and Simons (2004).

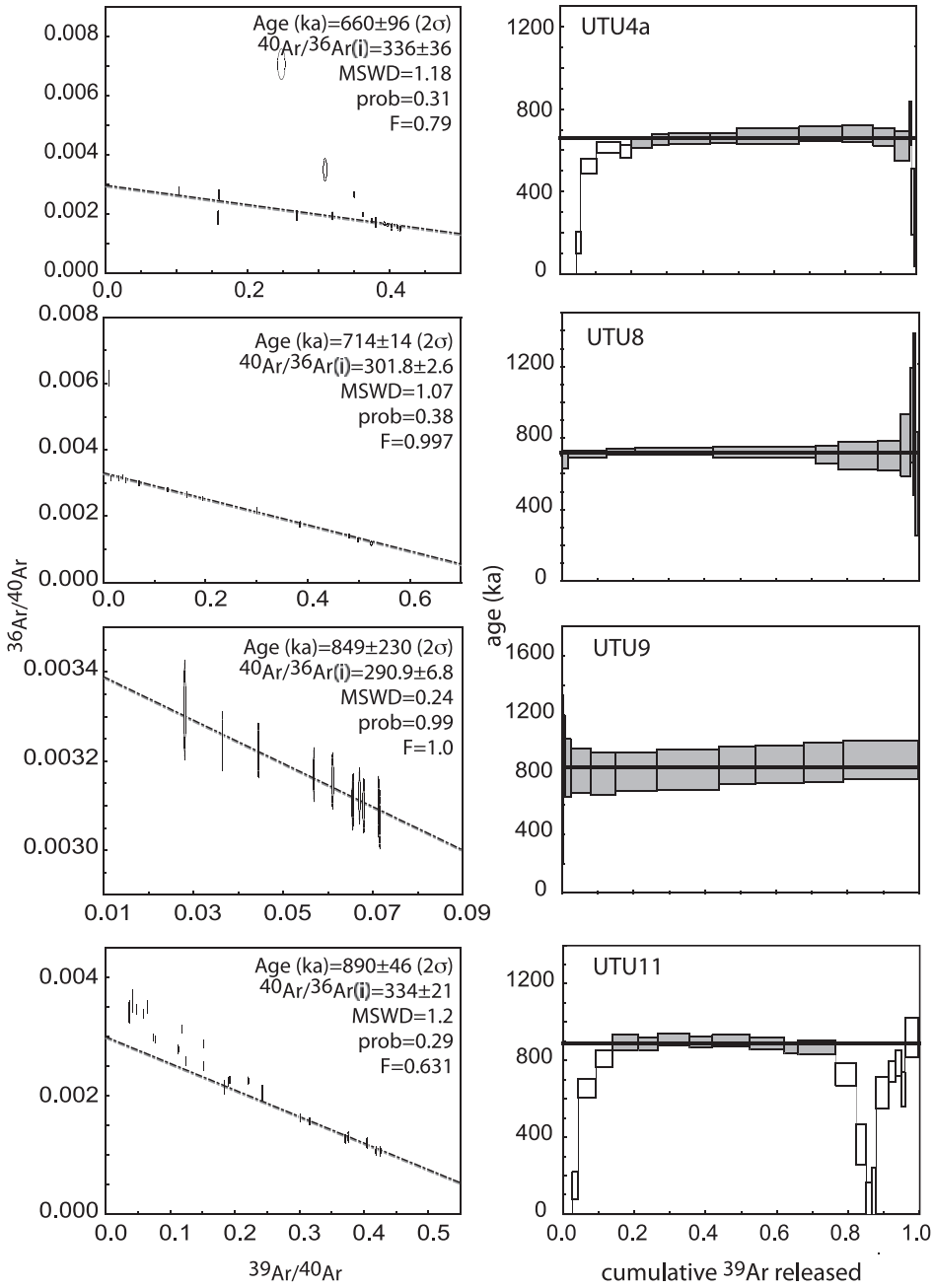

Fig. 5. Age spectra and inverse isochrons of eleven Uturuncu samples calculated using the plateau-chron function of the Isoplot 3.0 software (Ludwig, 2003). All data points and steps for each experiment are shown. Gray boxes indicate accepted plateau steps. Open ellipses and boxes show points excluded from the age calculation by Isoplot. The samples yield Pleistocene ages with mostly flat, undisturbed spectra. Some samples (4a, 11, 16, 28, 31) show disturbance in the low temperature steps, most likely associated with alteration. With the exception of sample UTU25, all samples show either an atmospheric or an elevated $^{40}Ar/^{36}Ar_i$ (trapped) component as expected. UTU25 shows a slightly lower $^{40}Ar/^{36}Ar_i$ and for this reason, 3 points from the regression were excluded to bring the $^{40}Ar/^{36}Ar_i$ within air values. However, using either method produces ages within error of each other, indicating that the age is robust.

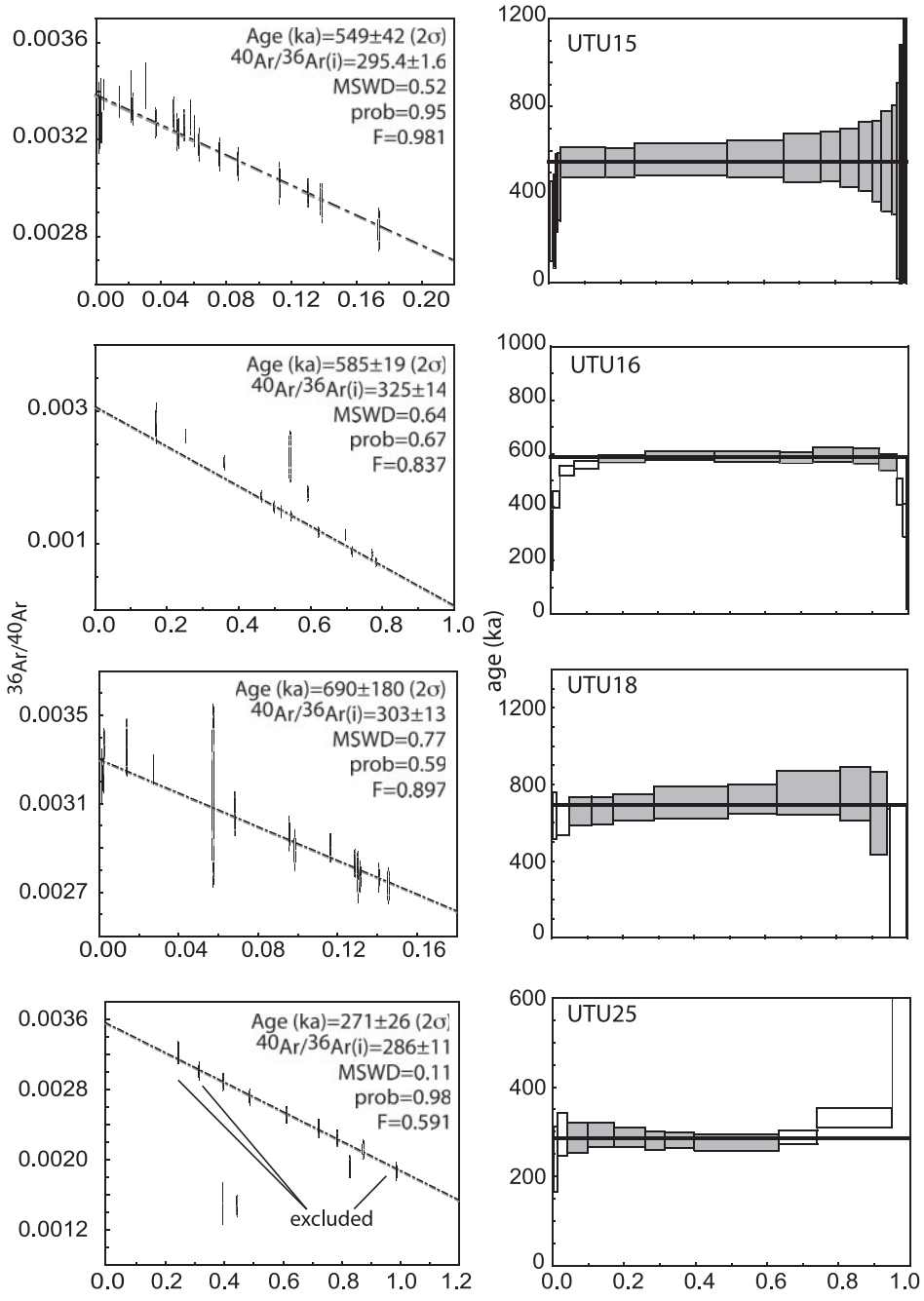

Fig. 5 (continued)

In summary, we find that differences in the assumed source geometry generate a larger range of accepted depths (~12–25 km below sea level or 17–30 km below local relief at 4 km above sea level) than variations in crustal elastic structure. The maximum source depths are among the deepest ever estimated using geodetic data. Given the

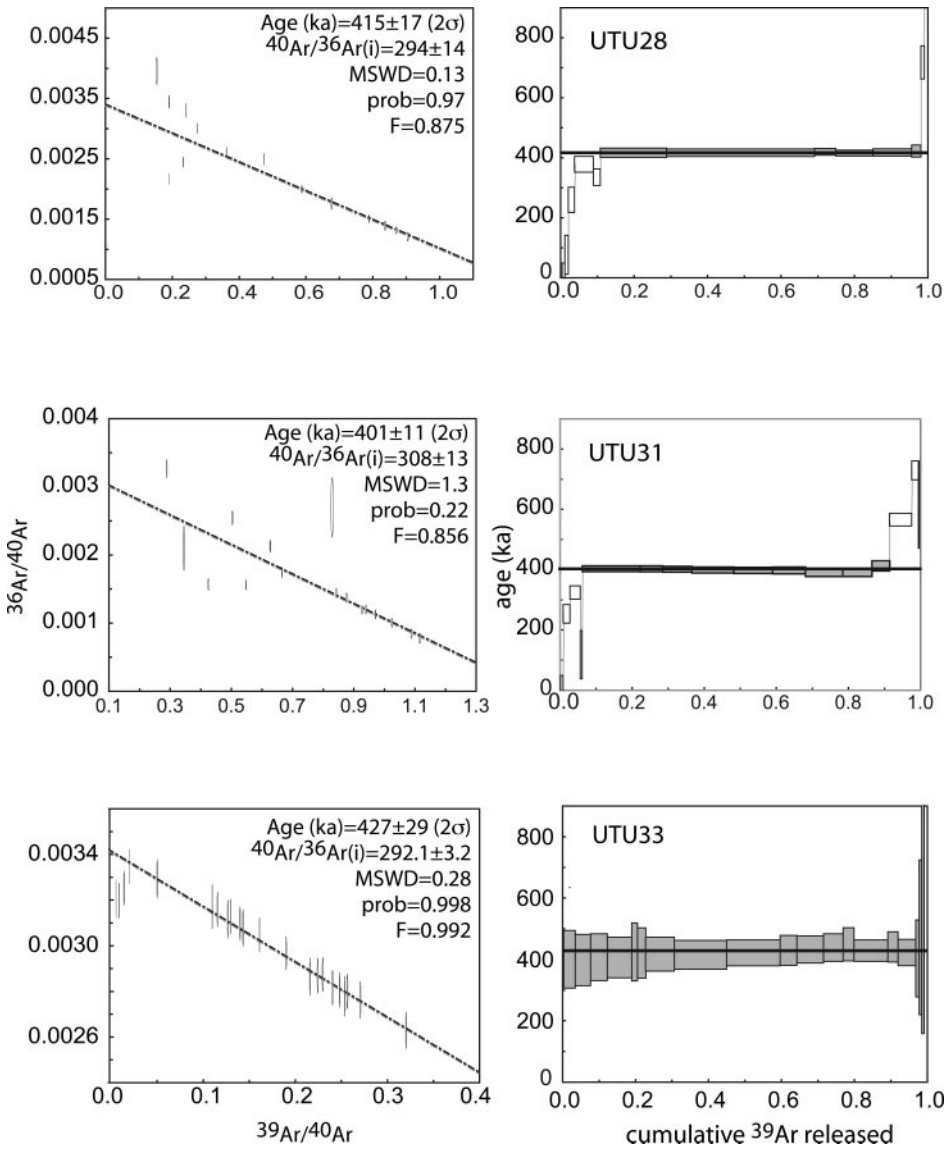

Fig. 5 (continued)

high temperatures in these regions, it is unlikely that deformation is purely "elastic" (see discussion in the next section). Local topographic variations can influence the inferred depth of a deformation source (for example, Williams and Wadge, 1998), but we find that, for Uturuncu, the effect of topography upon inferred source depth is less than other sources of uncertainty. The source of deformation is offset from the summit by 5 km to the west for all source geometries. Offsets of this magnitude are common at volcanoes of the central Andes and elsewhere (Pritchard and Simons, 2004).

The deformation is attributed to magma intrusion. Although hydrothermal systems can cause deformation they are not known to be located at depths of more than 10 km deep. The absence of a widespread hydrothermal system at Uturuncu and

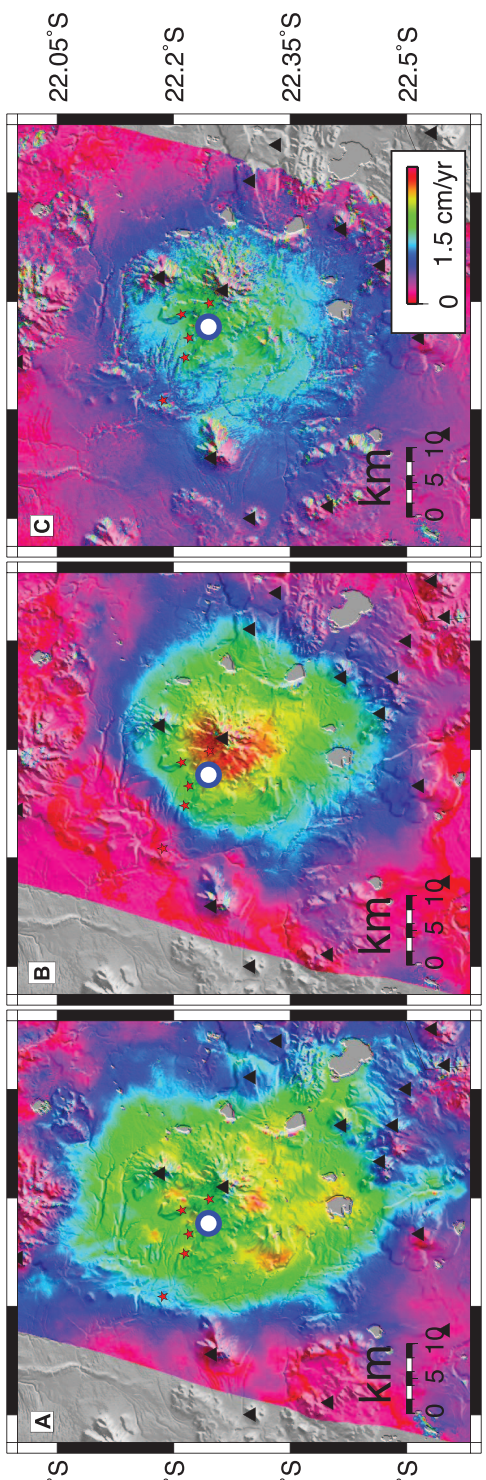

Fig. 6. Observed (A., B., C.) rates of deformation (cm/yr) at Uturuncu in three interferograms, from two different tracks of descending InSAR data. Locations where the seismometer was deployed during the April, 2003 field work are shown as red stars, and the blue/white circle shows the region of inferred seismic activity. Black triangles show volcanoes from the database of de Silva and Francis (1991) where the location of Uturuncu has been shifted to the east to correspond to the summit location.

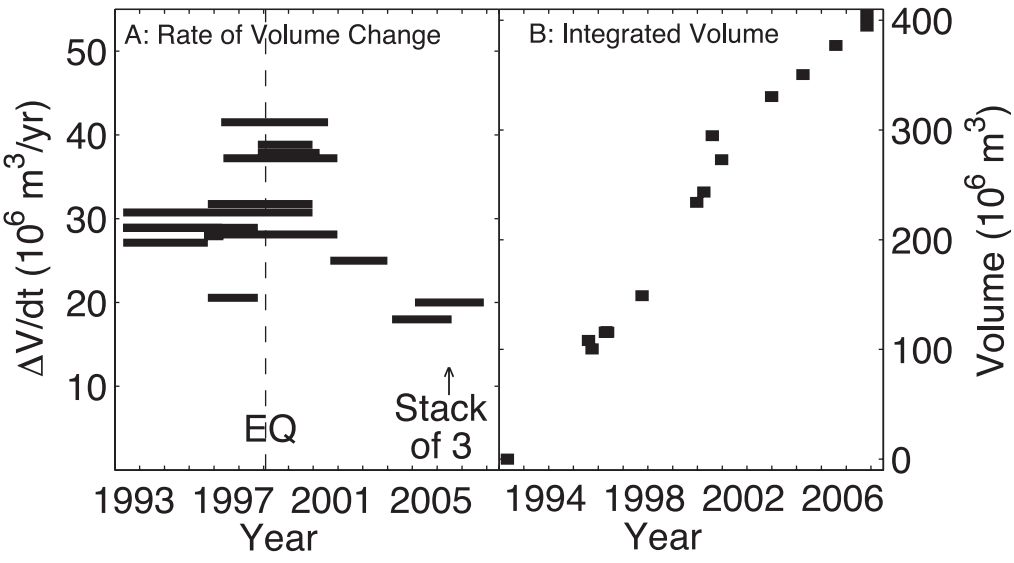

Fig. 7. (A) Inferred rate of volume change as a function of time, assuming a constant source depth, a spherical source in an elastic half-space, and a constant rate of deformation during the time period covered in the interferogram. The horizontal bar shows the time period covered by the interferogram. See Pritchard and Simons (2004) for a list of interferograms used. The time of a 1998 Mw 7.1 earthquake is shown as dotted line and labeled "EQ". (B) Volume inferred in a spherical point source magma chamber in a half-space as a function of time, assuming zero volume at the time of the first SAR image. We use the overlapping interferograms to do a linear least squares inversion for the volume change during the time interval between each SAR acquisition (for example, Lundgren and others, 2001), and assume that the deformation rate is constant during these intervals. We do not include error bars on (A) or (B) so as to not give a false sense of certainty – the largest errors are probably systematic and related to uncertainty in the rheology of the crust and magma. While we think the shapes of the plots are reliable the scales on the y-axes may not be.

the inferred deep source for deformation (>17 km) suggests a magmatic origin. Data from seismic arrays indicate that Uturuncu lies above a region of low seismic velocity and inferred partial melt, namely the Altiplano-Puna regional crustal magma body (Schmitz and others, 1997; Schilling and others, 1997; Chmielowski and others, 1999). The inferred depth and thickness of the seismically-imaged magma body are model dependent (Leidig and Zandt, 2003), but plausible depths are consistent with the source inferred to cause the InSAR deformation (>14 km below local relief; Leidig and Zandt, 2003). The interpretation of deformation is considered further after consideration of petrological constraints.

Time dependence of deformation and volume changes.—Using multiple interferograms, we constrain the time dependence of the rate of source volume change (fig. 7A) and the volume within the chamber as a function of time (fig. 7B). For simplicity, we assume a constant source depth using a spherical source in a half-space. We also assume that the deformation arises entirely as a consequence of a source volume change. For discussion of the possible effects of these assumptions, see Pritchard and Simons (2004). We previously suggested that an increase in the inferred rate of volume change in the magma chamber in 1998 might have been triggered by a Mw 7.1 earthquake in January 1998 (Pritchard and Simons, 2002, 2004). Now, with the additional data after 2000, it seems that the rate of inflation has diminished to its pre-1998 level (figs. 6 and 7). The total volume change over a period of 14 years is estimated at 400 x 10^6 m^3, giving an expansion of about 1 m^3/s.

Interpretation of the volume change rate is an open question. If the volume change is attributed to magma chamber replenishment, then the rate of magma

intrusion may be under-estimated, as magma intrusion will be partly accommodated by ductile deformation in the deeper parts of the crust or magma compressibility (for example, Johnson and others, 2000). However, volume changes can also occur by other processes not involving new magma influx, such as pressurization due to crystallization of water-saturated magma (Tait and others, 1989) or volume changes related to melting of crustal rocks. Furthermore, our volume may be an over-estimate if the effects of viscoelasticity are important, because a given volume change in the source causes greater deformation in a viscoelastic model than a purely elastic one (for example, Bonafede and others, 1986). A further complication arises if there is more than one magma chamber; a possibility that is allowed, but not required by the data. If there are stacked magma chambers that could be both inflating and deflating our volume estimates could be low (see the Magmatic Dipole section of Pritchard and Simons, 2004). On the other hand, if there are deep and shallow inflating sources, there are scenarios where our volume estimates could be too high.

Jellinek and DePaolo (2003) demonstrated that a magma chamber larger than a critical volume grows by ductile deformation of the walls. The critical volume depends on magma supply rate and rheology (and therefore temperature) of the crust. We estimate strain rates of 3×10^{-15} sec^{-1} for a spherical magma body of 100 km^3 volume inflating at 1 m^3/s for example. At such low strain rates hot rocks around and below the magma body are expected to deform by ductile mechanism, whereas the surface deformation is attributed to the elastic and viscoelastic response of the overlying colder brittle crust.

SEISMIC RECONNAISSANCE STUDY

We set up one portable seismic recording system at five different sites (figs. 8 and 9) at different times to sample the seismic activity of Uturuncu during April 1-6, 2003. The system used a Mark Products L4-C 1 Hz vertical geophone, a Pico Systems digitizer, a GPS clock, and recorded data on a laptop PC at a sample rate of 100 Hz. Seismic data were later displayed and analyzed using Matlab. The system was run for 2 to 14 hours at each site. The first station occupied was UTNW (fig. 9). Here, a surprisingly high number of 28 earthquakes were recorded in the first 2 hours of recording. All the events had clear P and S waves and are judged to be volcano tectonic (VT) events. Twenty-five of the events had the same S-P times of 1.2 sec (figs. 9, A, B, and C) and similar P-wave pulses with a period of 0.1 sec, followed by clear S waves with longer period and higher amplitude. We infer that these events all came from the same source or structure, inferred to be a fault at shallow depth. Slight variations in the S/P amplitude ratio (fig. 9) indicate that different parts of the structure were active. Two events had longer S-P times and came from different sources at greater distances from station UTNW. With data from a single station, however, we cannot determine the azimuth or depth for these events.

We took advantage of the fortunate circumstance of a persistent source by redeploying the seismic system at four other nearby locations, UTCA, UTBE, UTSU, and UTQU (fig. 8). In general the recorded rates were lower (0-5 per hr; mean for all stations 2.6 per hr), but we succeeded in recording at least one event at three other locations (figs. 9, D, E, F), which we infer came from the same source. Nearly all the events at each station had similar S-P times, suggesting again that the events came from mainly one source. We note that the initial P waves had similar appearances and characteristic periods of 0.1 sec at each of the other sites. The S-P times at UTNW, UTCA, and UTBE were all 1.1 to 1.3 sec, suggesting that the source was approximately equally distant from each of these stations. The site that fulfills this criterion is marked with an "X" in figure 8, and represents the epicenter. Because this site is ~3 km from each station, this also indicates that the P wave velocity is about 2.5 km/sec. This is a typical value observed at many volcanoes (McNutt, 2005), and may reflect a combina-

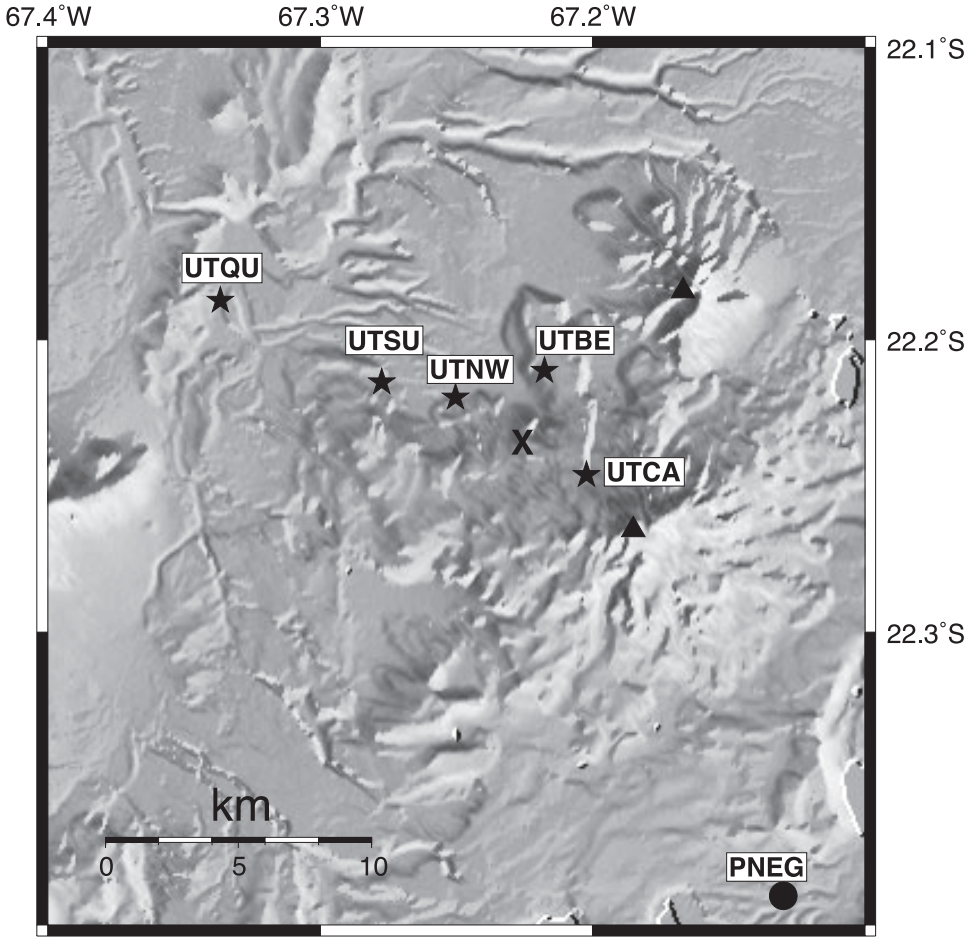

Fig. 8. Seismic station locations deployed in 2003 at Uturuncu volcano are marked as stars. The circle shows the station PNEG deployed by Zandt and colleagues in 1996-1997. "X" shows estimated source epicentral location. The triangles are volcanoes from the database of de Silva and Francis (1991) with the southern triangle being Uturuncu summit.

tion of lava flows and unconsolidated material (tephra and alluvium) near the surface. The depths of the earthquakes are likely 3 to 4 km, which is typical of values for many other volcanoes (McNutt, 2005), which we cannot determine uniquely from our data, and this implies that the shallow velocities are somewhat higher than 2.5 km/sec.

Magnitudes of the events were determined using the coda duration estimate of Lee and others (1972), which is appropriate because the bulk of the events came from the same source. The magnitudes were in the range 0.5 to 1.5. We made a plot of the cumulative number of events versus magnitude (fig. 10). Although there are only 40 events the *b*-value of the frequency-magnitude relation can be approximately estimated by linear regression at 1.04, which is near the worldwide average value of 0.9 to 1.0 for tectonic earthquakes. This suggests that the earthquakes are not affected by variations in heat, pore pressure, or material heterogeneity that characterize many volcanic areas (Wiemer and others, 1998; McNutt, 2005), but instead represent only brittle failure in response to tectonic stresses. The deformation center at depth NW of the summit of

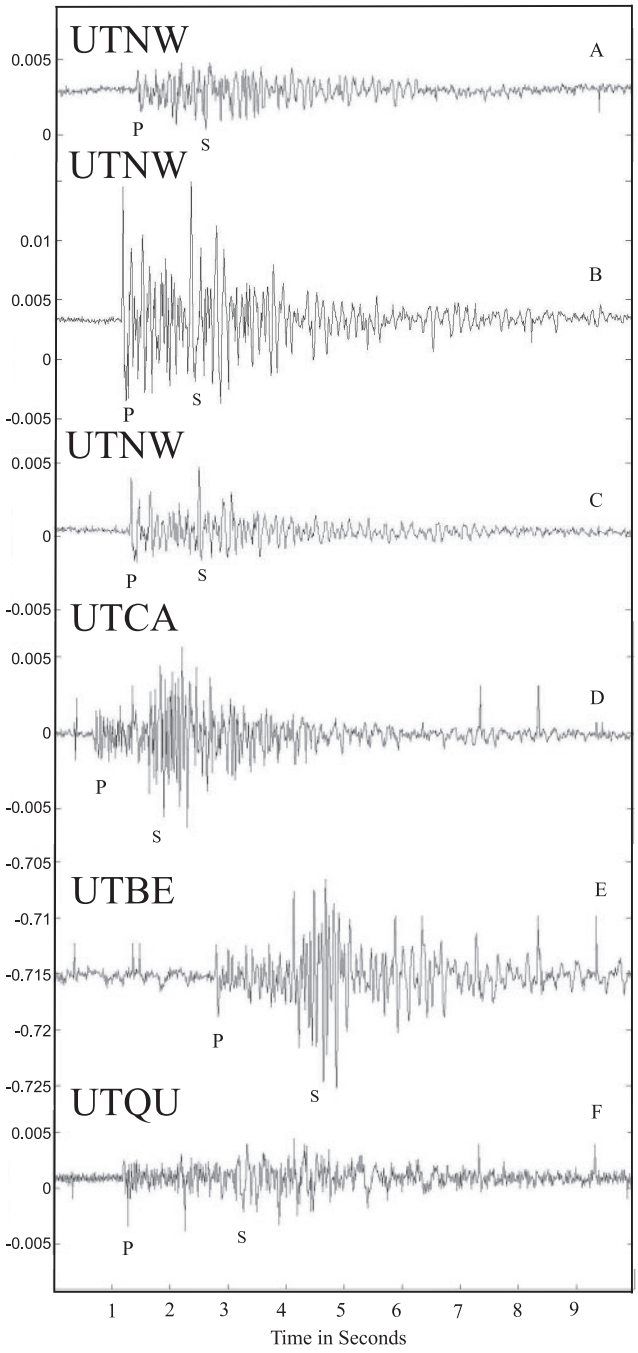

Fig. 9. Seismograms from stations UTNW (A, B, and C), UTCA (D), UTBE (E), and UTQU (F). Time is in seconds and amplitude is in arbitrary units. P and S arrivals are marked. Note the similar P wavelets for all stations, and the nearly identical S-P times of 1.2 seconds at UTNW. This suggests a restricted source region for the events. Noise spikes are present on several of the traces shown.

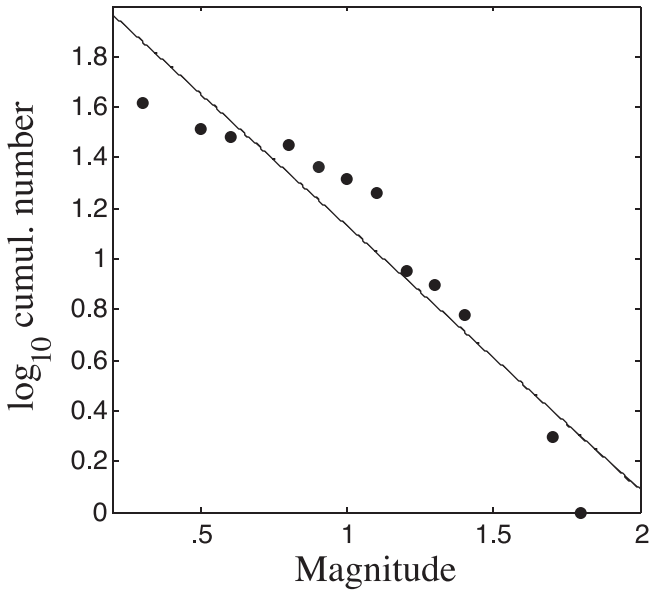

Fig. 10. Plot of the cumulative number of earthquakes versus magnitude. The slope or *b*-value is 1.04, suggesting that the swarm has the characteristics of tectonic activity. No involvement of magmatic fluids is suggested by this test.

Uturuncu is the obvious candidate for the source of tectonic stress. The surface projections of the deformation center and the estimated earthquake locations are within a few km of each other (figs. 6 and 8).

The station distances from the summit were: UTCA, 3.5 km; UTBE, 7.6 km, UTNW, 9.1 km, UTSU, 11.7 km, and UTQU, 18.7 km. The three closest stations provided the most critical data to determine the location of the identified persistent source. Other seismic stations have been operated in the vicinity of Uturuncu, notably a temporary network of regional stations as part of a PASSCAL study of the Altiplano-Puna magma body in 1996−1997 (Zandt and others, 2003). We examined data from station PNEG, 15 km SSE of Uturuncu for the period November 9-December 31, 1996 to determine whether the background rate has been persistently high at other times. We found zero to several events per day (mean 3 per day) that had S-P times of 1 to 3 sec, appropriate for Uturuncu to be the source, but we found only a few events consistent with the same source as shown in figure 8. Station PNEG is far enough away that only the larger events would be seen, so we did not find a rate as high as observed in April 2003. Our favored interpretation is that the volcano has a persistent moderate background seismicity with occasional bursts, one of which we were fortunate to catch with our temporary deployment. Clearly our understanding would benefit from a permanent seismic network; nevertheless, we have learned a great deal from the reconnaissance study.

GEOCHEMISTRY

Major Elements

Figures 11 and 12 show major element data for dacite lavas, andesite inclusions and xenoliths with data listed in tables 4A and 4B. The dacite lavas are high-K (fig. 11A) according to the classification of Gill (1981), plotting within the calc-alkaline field (fig.

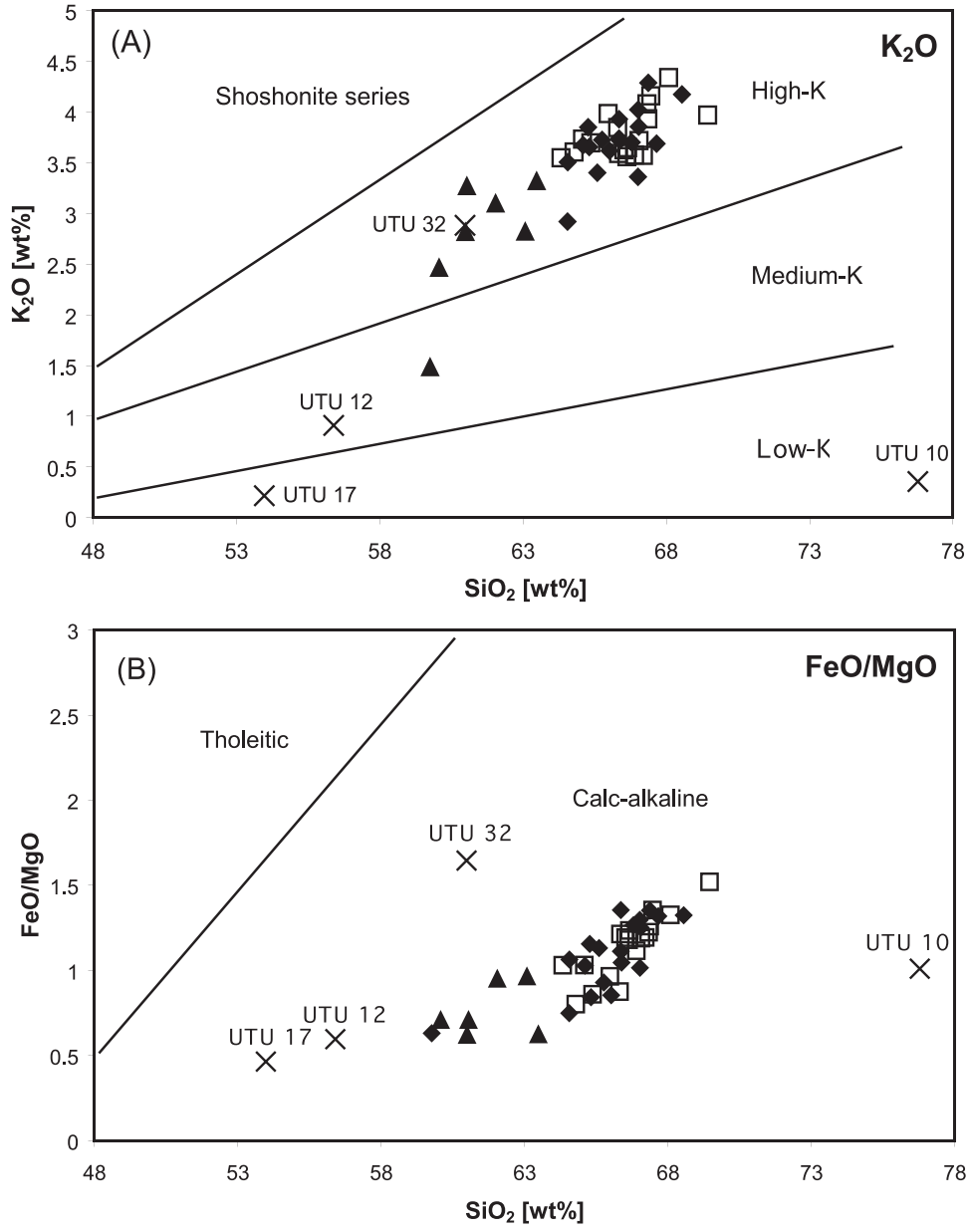

Fig. 11. Whole rock classification diagrams after (A) Gill (1981) and (B) Miyashiro (1974). Samples have been normalized to 100% volatile free with total Fe calculated as FeO. The Bolivian data come from analyses performed at the University of La Paz and can be found in Mayel Sunagua (2002). □ Bolivian data, ♦ lavas, ▲ Andesite inclusions, × xenoliths.

11B) of Miyashiro (1974). They show only minor variation in bulk composition, ranging from 62.3 to 66.8 percent SiO_2 (normalized to 100% volatile free). All andesite inclusions plot in the high-K, calc-alkaline fields, with the exception of one sample located in the medium-K field (fig. 11A). The andesite inclusions range from 57.3 to

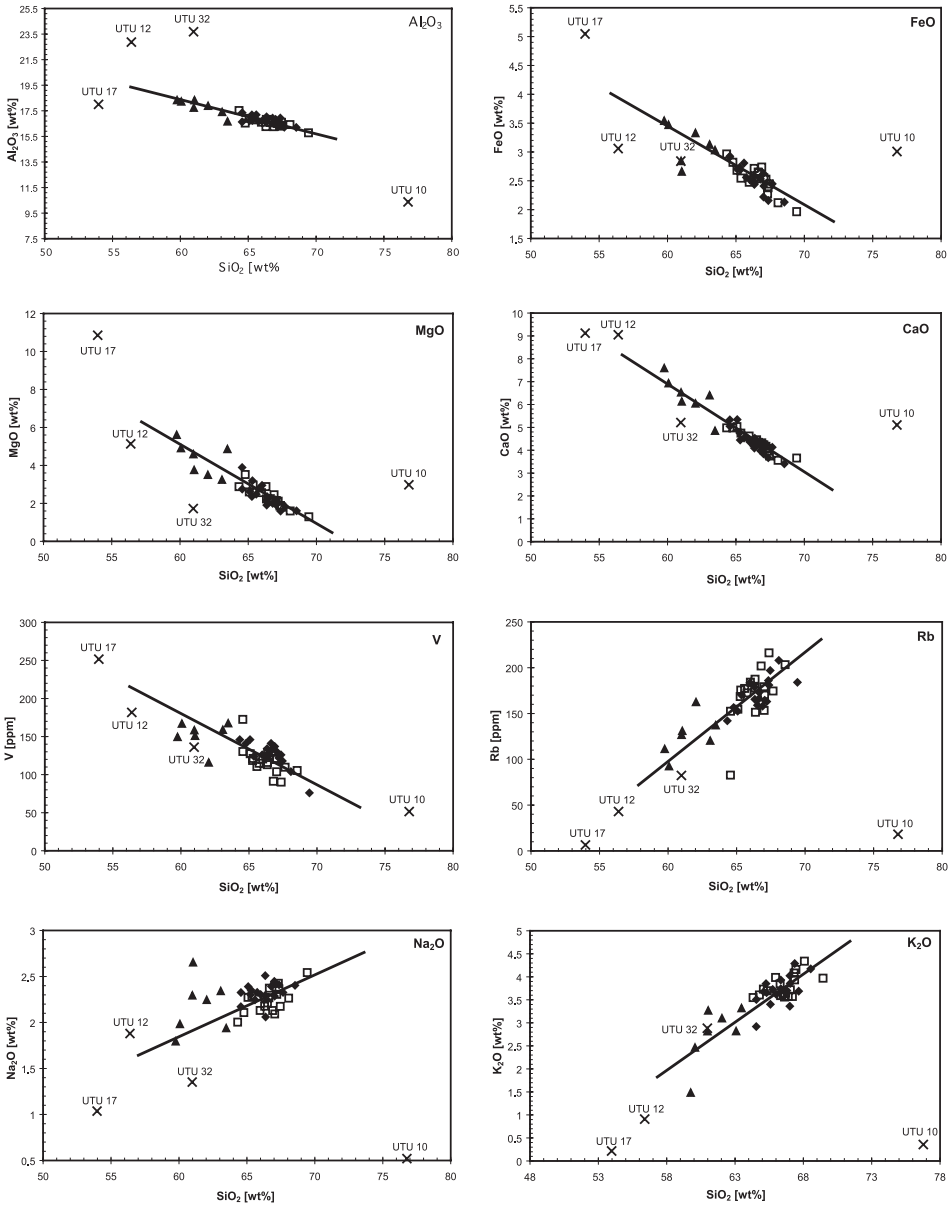

Fig. 12. SiO_2 versus selected other major and trace elements showing linear variations. There are negative correlations for Al_2O_3, MgO, CaO, FeO and V and positive correlations for Na_2O and K_2O with increasing SiO_2. Linear regressions are shown as solid lines. Xenolith samples plot away from these trend lines; UTU10: is quartzite with muscovite, hornblende and plagioclase; UTU12 and UTU17 are norite xenoliths; and UTU32 is a sillimanite-orthoclase gneiss. □ Bolivian data, ♦ lavas, ▲ Andesite inclusions, × xenoliths.

61.2 percent SiO_2. Andesite inclusions have higher Al_2O_3, CaO, MgO, FeO^T, MnO and lower K_2O abundances than the dacite lavas (table 4B). Lavas and inclusions plot along scattered and approximately linear trends on the major element variation diagrams

(fig. 12). The xenoliths include two norite samples (UTU 12 and UTU 17, 50.8 and 54.4 wt% SiO_2), a quartz-rich rock of igneous origin (UTU 10, 74.1 wt% SiO_2), and a sillimanite-orthoclase gneiss (UTU 32, 58.9% SiO_2) (fig. 12). A norite xenolith (UTU 35) with orbicular structure (Vernon, 1985) is also described, but its bulk-rock geochemistry was not analyzed.

Trace Elements

The dacite lavas, andesite inclusions and xenoliths have very high incompatible trace element abundances in agreement with previous studies of Andean volcanics (Kay and others, 1999). Nb, Zr, Th, Pb and La abundances are up to 10 times greater in these samples compared to other arc lavas such as those found, for example, in Santorini, Montserrat and the Mariana Arc (Elliott and others, 1997; Murphy and others, 2000; Mortazavi and Sparks, 2004). Feeley (1993) defined three zones across the arc with increases in incompatible elements to the east. The new Uturuncu data are consistent with his observations. Uturuncu lavas have higher incompatible element concentrations than volcanic rocks at the arc front of the Western Cordillera. Incompatible trace elements (Rb, Ba, Zr, U, Th and La) have higher concentrations in the dacite lavas compared to the andesite inclusions (for example Rb in fig. 12). In contrast, many compatible trace elements (V, Co, and Sc) have slightly lower concentrations in the dacite lavas compared to the andesite inclusions (for example V in fig. 12). Cu, Ni, Cr, Mo and Ga show no variation with increasing silica content.

PETROLOGY

Dacite Lavas

All lava samples are porphyritic (figs. 13A and 13B; table 3) with 40 to 60 volume percent phenocrysts (>300 μm and up to 7 mm) and microphenocrysts (>50 to <300 μm). The dominant phenocrysts are plagioclase (20–25%) and orthopyroxene (10–15 %). Other phenocryst phases are biotite (1−7%), quartz (1−6 %) and Fe-Ti oxides—ilmenite and magnetite (2−7 %). Apatite, clinopyroxene and amphibole are present in trace amounts in a few samples. The groundmass mineralogy (<50 μm) is very similar with both plagioclase and orthopyroxene as the dominant phases. The groundmass glass is high-SiO_2 rhyolite (75–79 wt% SiO_2) (table 4C).

There is a wide range of plagioclase compositions in the dacite lavas from An_{39}-An_{87} (fig. 14A). Three main plagioclase populations have been identified according to texture, composition and zoning profiles. Type 1 crystals are reversely zoned phenocrysts and microphenocrysts (fig. 13A) with cores of $An_{50\text{-}60}$ and thin calcic rims (50–200 μm wide) of An_{70-80}. The cores of many reversely zoned crystals have a dusty 'sieve' texture with great variation in anorthite content (between An_{50-65}) over distances of less than 5 μm. Type 2 crystals display oscillatory zoning of An_{65-85} throughout all or most of the crystal with individual zones 50 to 150 μm wide. Rims are typically ~An_{80}. Type 3 crystals are less common, dominantly unzoned smaller phenocrysts and microphenocrysts at An_{60}. A few crystals have normally zoned rims at An_{50-55}. Most lava samples contain all three types of plagioclase phenocrysts, though types 1 and 2 together account for >80 percent. Most plagioclase groundmass crystals are unzoned, with rare occurrences of slightly more calcic rims, similar to the larger type 1 phenocrysts described above.

Orthopyroxene accounts for 20 to 35 volume percent of the total crystal population, with sizes ranging from 10 μm groundmass crystals up to large phenocrysts, about 4 mm in diameter. Figure 14B displays the range of orthopyroxene compositions in the dacite lavas. All crystals are very Ca-poor at Wo_6 or less. Nearly all orthopyroxene phenocrysts show some zoning (figs. 13F and 13G). Four types were recognized. Type 1 crystals are reversely zoned phenocrysts and microphenocrysts with an Mg-poor core

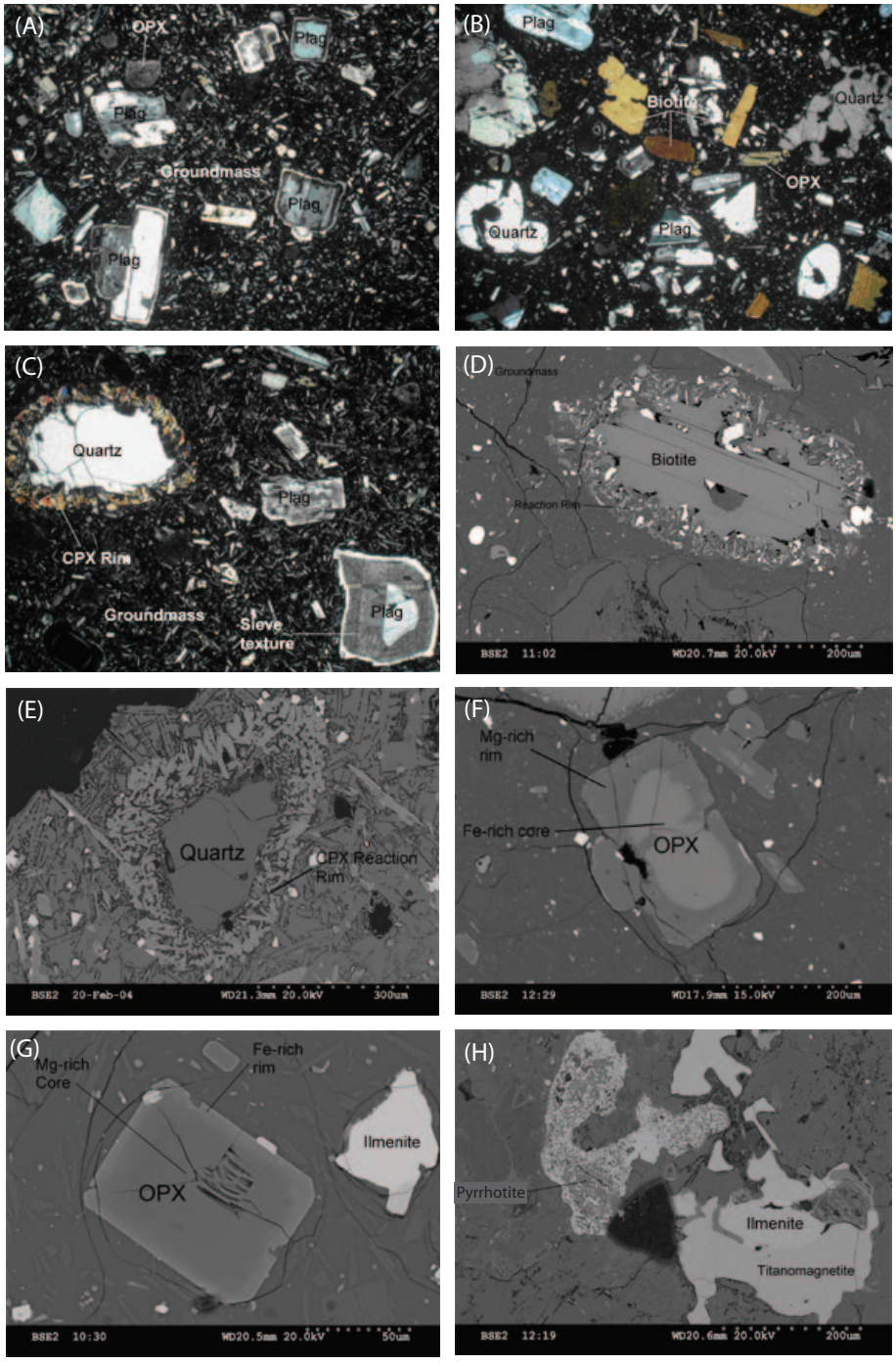

Fig. 13. Photomicrographs and back-scattered electron micrographs of dacite lava and andesite inclusions. Field of view in photomicrographs is 4 mm. (A) Coexisting Type 1 and Type 2 plagioclase phenocrysts in dacite lava. The type 2 oscillatory-zoned crystals contain dusty sieve-textured layers. (B) Dacite lava sample containing euhedral biotite phenocrysts and rounded quartz crystals. (C) Andesite inclusion with clinopyroxene reaction rim around quartz crystal and sieve-textured plagioclase crystal. (D) Dacite lava with reacted biotite rim comprising Fe-Ti oxides, opx and apatite. (E) Andesite inclusion sample showing clinopyroxene reaction rim around quartz. (F) and (G) Dacite lava with coexisting reversely zoned (f) and normally zoned (g) orthopyroxene phenocrysts. The darker parts of the crystals are Mg-rich. (H) Coexisting ilmenite and titanomagnetite in bottom right corner of lava dacite.

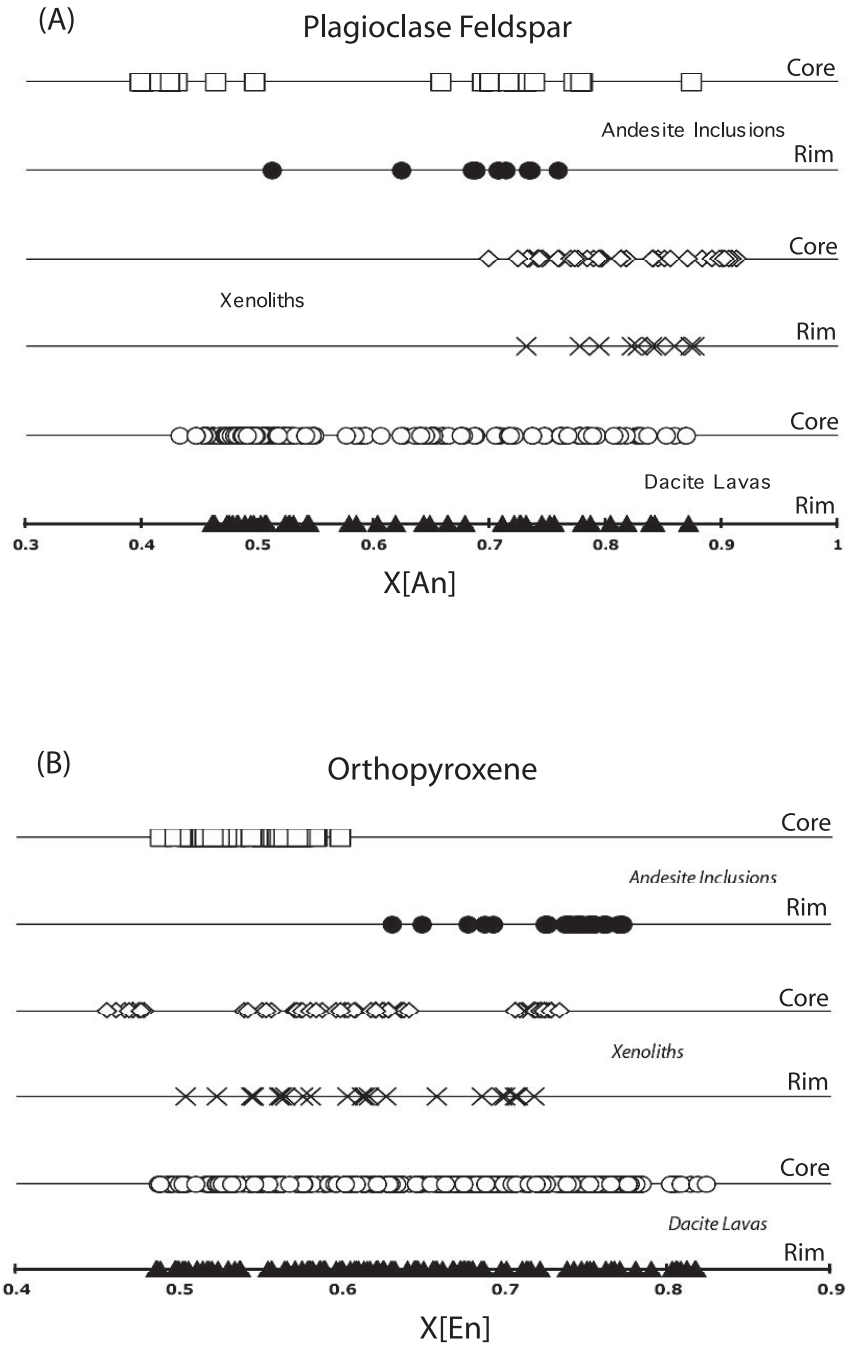

Fig. 14. (A) Anorthite content of plagioclase feldspar phenocrysts in andesite inclusions, xenoliths and dacite lavas. The upper line of symbols for each set represents plagioclase core compositions. Rim compositions are given by the lower line of symbols. Plagioclase in dacite lavas and andesite inclusions has a highly variable anorthite content between An_{40-85}. Xenoliths possess plagioclase feldspar phenocrysts that are consistently Ca-rich at An_{70-92}. (B) Enstatite content of orthopyroxene phenocrysts in andesite inclusions, xenoliths and dacite lavas. The upper line of symbols for each set represents orthopyroxene core compositions. Rim compositions are given by the lower line of symbols. Orthopyroxene in dacite lavas and xenoliths exhibits a variable enstatite content between En_{45-82}. Orthopyroxene phenocrysts in andesite inclusions show prominent reverse zoning with Fe-rich, En_{50-60} cores and Mg-rich, En_{62-78} rims.

(En_{55}) and a gradual increase in Mg-content towards a rim composition of $En_{65–75}$. Type 2 crystals have unzoned cores of ~En_{55} with only a thin, Mg-rich rim 50 to 150 μm thick at $En_{65–75}$ (fig. 13F). Type 3 phenocrysts have core compositions of En_{65-80} and are normally and continuously zoned to Fe-rich rims ($En_{50–70}$) (fig. 13G). Types 1 and 2 account for about 50 percent, and type 3 crystals about 40 percent of the total orthopyroxene phenocryst population in lava samples. Type 4 crystals are less common, unzoned crystals with a narrow compositional range, usually at low Mg contents ($En_{50–60}$). Groundmass orthopyroxene crystals are typically unzoned with $En_{50–60}$; SEM analyses suggest reversely zoned, darker rims with higher Mg-contents ($En_{60–70}$) in some samples.

Biotite is present in most dacites, accounting for 1 to 10 volume percent of phenocrysts. The majority of crystals are euhedral, with lengths between 200 μm and 2.5 mm and widths between 50 μm and 1 mm. Biotite has reaction rims consisting of Fe-Ti oxides, orthopyroxene, apatite and zircon (fig. 13D). Some biotites also contain intergrowths of plagioclase feldspar and small, rounded crystals of monazite. All biotite phenocrysts in lava samples are relatively Mg- and Si-poor with 34−37% SiO_2 and Fe-rich relative to the xenoliths, which are at $Fe_{18–24}$.

Quartz (1–6% crystal content) occurs as large phenocrysts ranging between 300 μm and 2 mm in diameter. The crystals are highly rounded with eroded embayments with pronounced cracks, commonly filled with rhyolitic glass (fig. 13B).

Fe-Ti oxides account for between 1 and 5 volume percent of the total crystal content in dacite lavas and occur as small rounded microphenocrysts and groundmass crystals. Many titanomagnetite and ilmenite (>80 vol% of oxides) crystals are in contact with each other (fig. 13H); magnetite (<20 vol%) commonly exhibits fine-scale lamellar exsolution textures.

Matrix glass compositions have high silica-rhyolite compositions: 77.7−79.2 wt% SiO_2, 11.5−13.2 wt% Al_2O_3, 5.8−6.8 wt% K_2O, and 1.2−2.2 wt% Na_2O. Small amounts of apatite, pyrrhotite (fig. 13H), monazite, and zircon were observed, commonly as inclusions within biotite phenocrysts or as small microlites within the groundmass.

Andesite Inclusions

The andesite inclusions have a similar mineral assemblage to the dacite lavas with plagioclase (20−35 vol%) and orthopyroxene (10−20 vol%) phenocrysts and microphenocrysts (table 3). The other mineral phases are biotite (1−4 vol%), Fe-Ti oxides (1−2 vol%), clinopyroxene (1−2 vol%), quartz (<1 vol%) and amphibole (<1%). These inclusions have a higher proportion of phenocrysts and microphenocrysts (50−65 vol%) than the dacite host lavas (figs. 13C and 13E), with a relatively crystalline groundmass (35−50 vol%).

Plagioclase feldspar accounts for 40 to 65 percent of the total crystal population and ranges in size from small groundmass crystals <30 μm in length to large phenocrysts ~4 mm in length. There is a similar distribution of reverse (type 1) and oscillatory (type 2) plagioclase crystals in the andesite inclusions and lava samples, but also a greater proportion of normally zoned phenocrysts with cores at An_{75} and rims at An_{65}. Type 1 and 2 crystals each account for about 20 percent of the total plagioclase phenocryst population, with the normally zoned crystals comprising about 60 percent.

Orthopyroxene is a major constituent of andesite inclusions, accounting for 20 to 35 percent of total crystal content with a similar size range as that described for plagioclase feldspar above. All crystals analyzed exhibit strong reverse zoning with Fe-rich cores at $En_{50–60}$ surrounded by Mg-rich rims at $En_{70–80}$ (fig. 14B). There is some variation between samples concerning the width of unzoned cores, with most samples falling somewhere between types 1 and 2 as described in the dacite petrology above.

Clinopyroxene is present in small amounts (<5%), with a fairly uniform composition of En_{44}- Wo_{37} - Fs_{18}. Some phenocrysts show slight reverse zoning with Fe-rich cores at En_{43-44} and Mg-, Ca-rich rims at En_{45-46}. There are also small clinopyroxene microphenocrysts forming reaction rims around quartz crystals (figs. 13C and 13E) with a similar composition to the other clinopyroxene crystals.

Fe-Ti oxides amount to 1 to 10 percent of the total crystal population, compared to 1 to 5 percent in dacite lavas. The distribution is almost exclusively ilmenite and titanomagnetite with very minor amounts of magnetite that is altered and very heterogeneous in composition. The ilmenite and titanomagnetite microphenocrysts lacking exsolution textures are commonly found in contact.

Matrix glass compositions are high silica rhyolites (table 4C): 77.7 wt% SiO_2, 11.6 wt% Al_2O_3, 6.1 wt% K_2O and 1.5 wt% Na_2O. Small amounts of apatite, pyrrhotite, monazite, and zircon were found in andesite inclusions, usually as inclusions within biotite phenocrysts or as small microlites within the groundmass.

Xenoliths

The two norites (UTU 12 and UTU 17) are holocrystalline, coarse-grained (>200 μm in diameter) rocks (figs. 15A and 15G) with plagioclase (40−55 vol%), orthopyroxene (35−50 vol %) and the remainder (<10%) consisting of biotite, Fe-Ti oxides, apatite, with trace amounts of quartz and clinopyroxene. Small inclusions of norite (fig. 15B), containing plagioclase and orthopyroxene with similar compositions to the large norite xenoliths, are also found in many dacite lavas. They have adcumulate textures. Plagioclase is highly calcic, with both cores and rims between An_{75-95} (fig. 14A). There is a paucity of oscillatory-zoned crystals, with reverse zoning dominating (cores An_{75} and rims An_{85-90}). Some normally zoned phenocrysts are observed with calcic cores at An_{90} surrounded by more sodic rims at An_{80}.

Orthopyroxene is relatively Mg-poor at <En_{74}. ~50 percent of analyzed orthopyroxene phenocrysts are normally zoned (similar to type 4 crystals in lava samples above), with a Mg-rich core at En_{75}, becoming continuously Mg-poor towards a rim composition of En_{65} (fig. 14B). Unzoned orthopyroxenes, (En_{65-70}), and reversely zoned phenocrysts with a Mg-poor core at En_{45} grading up to a rim composition of En_{55}, are occasionally seen in some samples.

The orbicular xenolith (UTU 35) consists of a core of orthopyroxene and plagioclase crystals surrounded by alternating concentric layers (fig. 15F) of fine-grained plagioclase (0.5 mm thick) and thicker layers (1.5 mm) of radial orthopyroxene and biotite. The unzoned plagioclase is highly calcic (An_{85-90}). Orthopyroxene crystals show weak normal zoning with En_{60-70} cores surrounded by En_{55-60} rims. The true 'core' or interior of this orbicular norite xenolith exhibits orthopyroxene compositions of En_{70} compared with the surrounding concentric layers at En_{55-65}. Biotite in the concentric layers is more Fe-rich (Fe_{20-22}) than other xenolith samples (Fe_{11-16}).

The quartz-rich igneous xenolith (UTU 10) contains 50 to 65 percent modal quartz, 25 to 35 percent plagioclase feldspar, and small amounts of orthopyroxene (fig. 15C), and traces of clinopyroxene, Fe-Ti oxides, zircon and biotite (fig. 15F). Quartz grains are very well rounded with a high sphericity and a polymodal size distribution from 50 μm to 1 mm diameter. Plagioclase is more calcic than other xenolith samples at ~An_{90}.

The coarse sillimanite-orthoclase gneiss xenolith (UTU 32) contains 80 percent sillimanite and alkali-feldspar as the dominant constituents. Sillimanite occurs as large, elongate, commonly acicular grains ~500 μm to 2 mm in length and also many smaller, broken-down, highly acicular forms, from 50 to 300 μm in length. Alkali-feldspars range from 300 μm to 1 mm in diameter and are rounded with faint exsolution textures. Other phases present are occasional rounded quartz crystals, rutile (TiO_2) infilling gaps and small, round opaque ilmenite microphenocrysts. Much

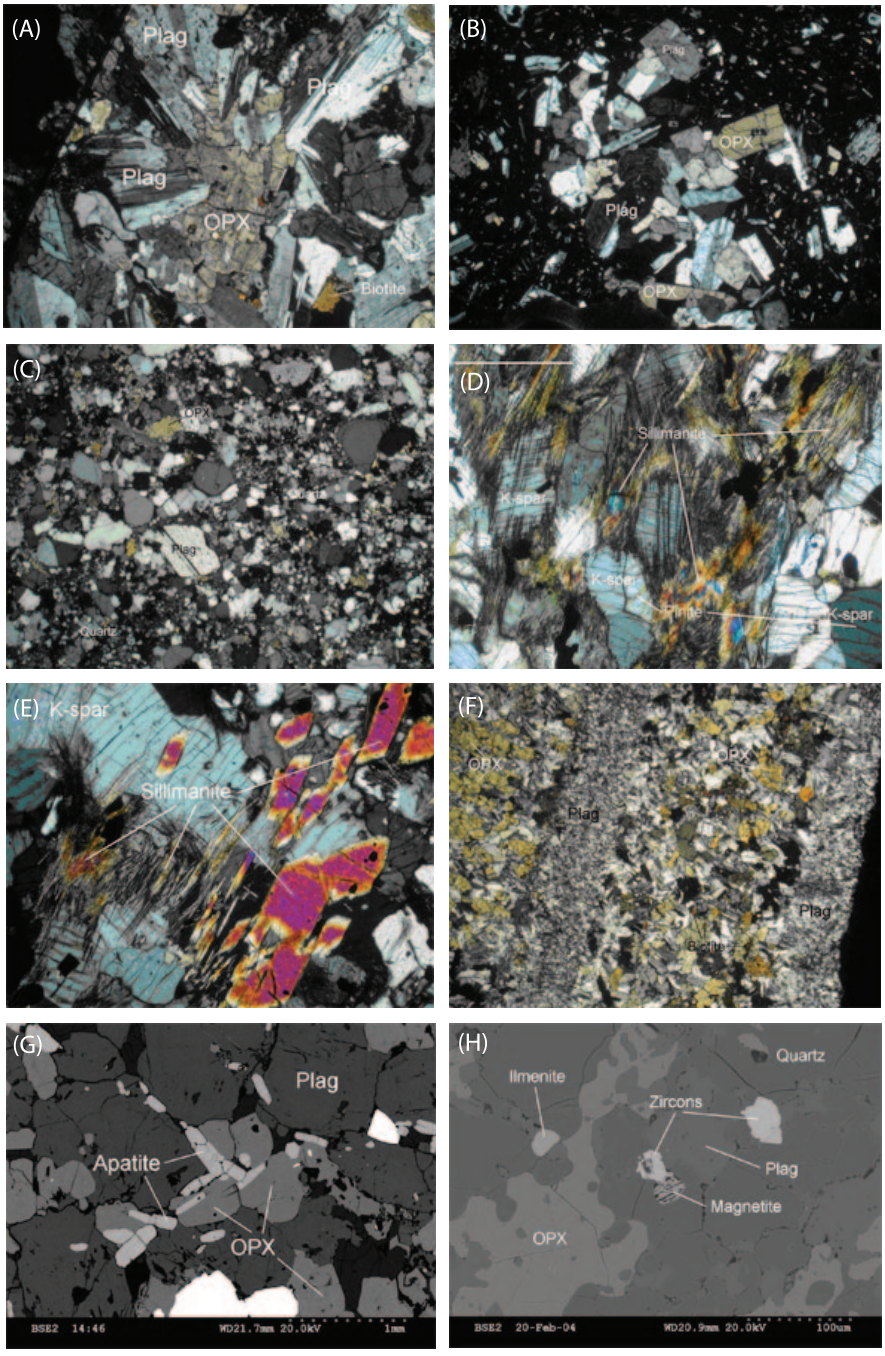

Fig. 15. Photomicrographs and back-scattered electron micrographs of Uturuncu xenolith samples. Field of view in photomicrographs is 4 mm. (A) Orthopyroxene and plagioclase feldspar crystals in cumulate norite sample (UTU 12). (B) Norite inclusion in dacite lava (UTU 18). (C) Polymodal quartz crystals in quartzite xenolith (UTU 10). (D) Sillimanite gneiss (UTU 32) contains fine-grained fibrous sillimanite crystals co-existing with orthoclase and quartz crystals permeated by yellow/green pinnite. (E) Large sillimanite crystal (UTU 32) is partly broken down to smaller forms. (F) Orbicular norite xenolith (UTU 35) with alternating concentric layers of lighter plagioclase and darker orthopyroxene and biotite. (G) Norite xenolith (UTU 17) with quartz (black), plagioclase (dark gray), orthopyroxene (light gray), ilmenite (white) and elongated apatites. (H) Zircons (light gray/white) and magnetite with exsolution lamellae in quartzite xenolith (UTU 10).

of the sample is permeated by yellow-green amorphous chlorite and muscovite (figs. 15D and 15E).

Melt Inclusions

Melt inclusions occur most commonly in orthopyroxene, plagioclase and biotite. Inclusions containing crystals, bubbles or having cracks running through them were excluded from analyses. Melt inclusions have rhyolite compositions (table 4D): 68.3−77.4% SiO_2 with 1.6−3.5% Na_2O, 10.4−17% Al_2O_3 and 4.3−7.4% K_2O, with anhydrous totals of 94.7–98.5 wt%. Volatile contents (other than water) are all low: <0.33% F, <0.08% SO_2, <0.21% P_2O_5 and <0.32% Cl.

ESTIMATES OF INTENSIVE MAGMA PARAMETERS

Temperature and fO_2

As described above, compositions of normal and reversely zoned orthopyroxene crystals commonly converge at the rim. Rim compositions of orthopyroxene and touching Fe-Ti oxides were therefore used to estimate the T, fO_2 conditions of the magmas, using QUILF (Andersen and others, 1993). The compositions used met the equilibrium conditions specified by Bacon and Hirschmann (1988). Calculated temperatures and oxygen fugacities are given in table 5. In many lava samples, both normally and reversely zoned orthopyroxene phenocrysts are present, and so caution must be taken when differentiating between core and rim temperatures and fO_2. In the dacite lavas (table 5), temperatures estimated using orthopyroxene rim compositions range from 813 − 886 ± 20°C (average 838 °C, n = 7); orthopyroxene core compositions give temperatures in the range 796 – 858 ± 20 °C (average 835 °C, n = 5). Orthopyroxene compositions from the andesite inclusions give much higher temperatures (table 5), for example, 987 °C (rims) and 970 °C (cores). $Log_{10}(fO_2)$ in the dacite lavas ranges from −12.3 to −13.6 (average −13.0), compared with $\log_{10}(fO_2)$ −8.5 to −10.6 in the andesite inclusions. These values equate to QFM + 0.3 to 1.4 log units. The associated uncertainties are up to ~1 $\log_{10}$ unit for $f(O_2)$ (Murphy and others, 2000).

Phase Equilibria

The Uturuncu mineral assemblage is dominated by orthopyroxene, plagioclase and biotite, with little or no amphibole. Experiments on the Mt Pinatubo dacite indicate that increasing fO_2 favors crystallization of Fe-Ti oxides and more Mg-rich orthopyroxene and biotite over amphibole (Scaillet and Evans, 1999). At the temperatures estimated for Uturuncu, biotite is typically found experimentally in very oxidized conditions, for example >NNO+3 (Costa and others, 2004), much higher than estimated from Uturuncu lavas (NNO +0.3 to +1.4). This discrepancy can be explained by the addition of only 1 percent sulphur, which reduces the stability of hornblende and allows biotite to become the dominant ferromagnesian phase (Costa and others, 2004). The presence of S-bearing phases (apatite and pyrrhotite) in the Uturuncu lavas is consistent with this interpretation. Anhydrite is absent (compare Costa and others, 2004), consistent with oxygen fugacities below the anhydrite stability field (NNO+1 to 1.5, Carroll and Rutherford, 1987). Biotite is stabilized by the high K_2O contents (>3.8%) of Uturuncu magmas (Costa and others, 2004). The high-An plagioclase may reflect crystallization from H_2O-rich melts (Arculus and Wills, 1980; Johnson and Rutherford, 1989; Sisson and Grove, 1993).

H_2O Contents

H_2O contents of rhyolitic melt inclusions (table 4D) were estimated by the difference method from electron micro-probe analysis of melt inclusions, with an

TABLE 5

Temperature and $f(O_2)$ data from QUILF geothermometry for dacite lavas, andesite inclusions and xenoliths

Dacite Lavas	T (°C)	log (fO_2)	ΔFMQ	Fe^{3+}/Fe^{2+}
UTU 21 RIM (En47)	846	-12.7	0.8	0.17
UTU 28 RIM (En70)	831	-13.0	0.8	0.16
UTU 22 RIM (En59)	840	-13.3	0.5	0.13
UTU 22 CORE (En44)	832	-13.4	0.4	0.14
UTU 38 RIM (En81)	837	-12.8	1.1	0.16
UTU 38 CORE (En56)	796	-13.6	0.9	0.18
UTU 25 CORE (En81)	833	-13.0	0.3	0.15
UTU 25 RIM (En68)	819	-13.4	0.6	0.15
UTU 4 RIM (En80)	886	-12.2	0.5	0.13
UTU 4 CORE (En60)	855	-12.7	0.6	0.15
UTU 4 Xen (En51)	823	-13.2	0.7	0.16
UTU 18 CORE (En71)	858	-13.0	0.2	0.12
UTU 18 RIM (En57)	813	-13.4	0.5	0.17
Andesite Inclusions				
UTU 2 RIM (En79)	988	-8.5	1.3	0.31
UTU 2 CORE (En52)	973	-10.6	0.9	0.14
UTU 2 RIM (En75)	985	-8.8	1.1	0.29
UTU 2 CORE (En56)	966	-10.5	1.0	0.16
Xenoliths				
UTU 10 RIM (En52)	551?	-18.2	3.3?	
UTU 12 RIM (En62)	467?	-19.2	5.7?	

Fe^{3+}/Fe^{2+} ratios are calculated using Kress and Carmichael (1991).

uncertainty of ~0.6 weight percent (Devine and others, 1995; Humphreys and others, 2006a). H_2O contents range from 1.4 to 5.3 weight percent, with no clear relationship between dacite lavas, andesite inclusions and xenoliths. Melt inclusions in plagioclase showed the widest range of H_2O (1.5–5.3 wt%), compared with orthopyroxenes (2.1–4.3 wt%) and biotite (2.8–4.6 wt%). These values of H_2O suggest crystallization

water pressures of up to 170 MPa, assuming H_2O-saturated rhyolite melt containing 5.3 weight percent H_2O, using the solubility relationship of Newman and Lowenstern (2002). This estimate, however, assumes that there are no other major volatile components (for example, CO_2), and therefore represents a minimum upper bound pressure. The minimum storage depth for the magma is therefore estimated at ~6.5 km.

ORIGIN OF XENOLITHS

The mineral assemblages and mineral compositions of the norite nodules are similar to the phenocryst assemblages in the andesites and dacites, suggesting that they crystallized from similar magmas. The highly calcic plagioclase would be consistent with precipitation either from melts at high pH_2O (Arculus and Wills, 1980; Sisson and Grove, 1993) or from melts that are hotter and less evolved than any of the andesite inclusions. We therefore suggest that these nodules represent adcumulates of early-formed crystals that segregated from residual melt. Formation of orbicular structures requires a lack of nuclei in the magma, forcing crystallization to occur only on solid objects (Vernon, 1985).

The quartz-rich igneous xenolith has a granular texture. These attributes imply cataclastic deformation of an unusually quartz-rich igneous precursor. One explanation is that these xenoliths represent the residue after partial melting of a rock on the quartz-rich side of the granite minimum in Petrogeny's residua system (Tuttle and Bowen, 1958). In such bulk compositions melting preferentially extracts feldspar components leaving a quartz-rich residuum. The presence of orthopyroxene, anorthite (An_{90}), zircon, trace clinopyroxene and oxide is consistent with remelting of plutonic rocks with close affinities to the Uturuncu volcanic suite and norite. The precursor needs to have had significant quartz indicating a plutonic rock more evolved (granodiorite) than the norites.

The sillimanite-orthoclase gneiss formed by high-grade regional metamorphism. The ubiquitous occurrence of the alteration product pinite means that the xenoliths have been heated to temperatures in excess of 450°C and pressures of over 500 MPa (Ague and others, 2001). The presence of fibrolite needles replacing earlier large sillimanite crystals, and the unusual assemblage dominated by orthoclase can be attributed to partial melting (J. Ague, personal communication). This xenolith could represent a piece of old, regional metamorphosed basement, perhaps a fragment of Pre-Cenozoic basement in the Altiplano and Puna complexes (Allmendinger and others, 1997).

MAGMA MIXING PROCESSES

Many petrological features of the dacites indicate disequilbrium due to the effects of magma mixing. The complex zoning in the plagioclase feldspars and the intermingling on a small scale of feldspars with independent histories are typical features of orogenic andesites and dacites (Anderson, 1976; Clynne, 1999; Murphy and others, 2000; Mortazavi and Sparks, 2004; Humphreys and others, 2006b). The mixed plagioclase populations can be explained by convective mixing caused by direct mixing with more mafic magma or self-mixing caused by heat transfer from hotter magmas (Anderson, 1976; Sparks and others, 1977; Couch and others, 2001). Complex plagioclase zoning patterns and textures can be ambiguous as they may arise from changes of temperature, water pressure or melt composition. However, the occurrence of normal and reversely zoned orthopyroxene crystals, with rim compositions converging on the same value (~En_{65}), is a signature of magma mixing (Luhr and Carmichael, 1980). The rim convergence indicates that two different magmas have come into contact and equilibrated with each other so that late-stage rim growth is at the same composition. Some lava samples (for example UTU 38) contain many different

orthopyroxene crystal compositions; this may reflect derivation from different parent melts. UTU 38 also exhibits reverse zoning in orthopyroxene, but the rims have different compositions and do not appear to have equilibrated, suggesting short times between mixing, eruption and quenching. An important role for magma mixing is also indicated from the ubiquitous andesite inclusions and evidence for their break up to form a xenocryst component in the dacites. For example, some plagioclase crystals in dacite lavas have high-Fe rims (fig. 16) and are likely to represent xenocrysts from broken-up andesite inclusions, incorporated into the dacite lava as magma mixing ensued. Other xenocrystal components are related to disruption of norite cumulates into the dacite.

Although magma mixing is clearly implicated, some of the disequilibrium features could also be a consequence of decompression and degassing. Resorbed quartz with clinopyroxene reaction rims and sieve textured, sodic cores to type 1 plagioclase phenocrysts could result from either process (Nelson and Montana, 1992). Oscillatory zoning in plagioclase phenocrysts is likewise ambiguous to interpret as it can result from temperature or pH_2O fluctuations that could arise from thermal convection (Couch and others, 2001; Ginibre and others, 2002), heating due to decompression-induced crystallization (Blundy and others, 2006) or pressure changes induced by eruption (Melnik and Sparks, 2005; Humphreys and others, 2006b). Temperature estimates in the range 796 to 886°C for the dacites indicate large thermal fluctuations.

Some petrological observations suggest a role for changes in redox conditions. Firstly, the andesite inclusions contain orthopyroxene crystals with pronounced reverse zoning, but normal magmatic differentiation and magma mixing with more evolved, silicic melt should produce normal zoning (Mg-rich cores, Fe-rich rims). However, increasing fO_2 favors the crystallization of Mg-rich orthopyroxene (Scaillet and Evans, 1999). The reverse zoning therefore suggests more oxidizing conditions during crystallization of orthopyroxene rims in the andesite. Secondly, the cores and

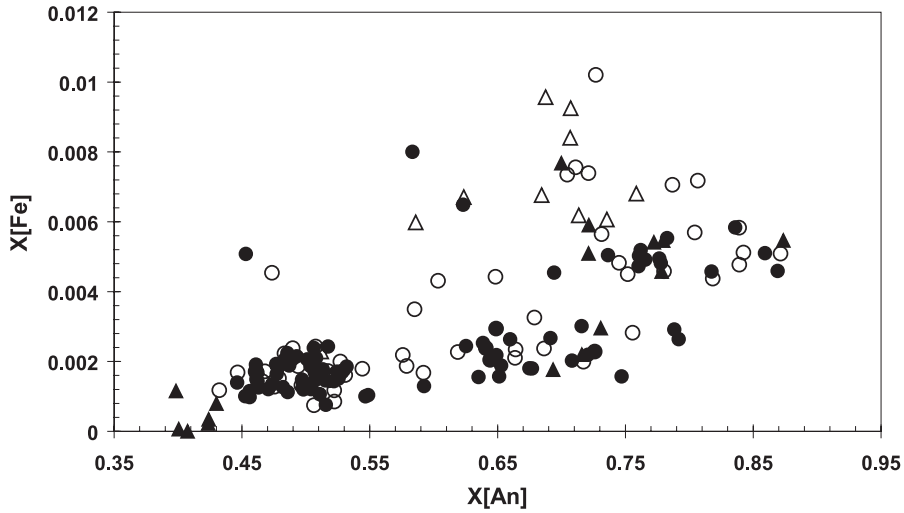

Fig. 16. A plot of $X_{[Fe]}$ vs. X_{An} content for lava samples and andesite inclusions. As X_{An} increases, the Al-content of the plagioclase increases, allowing the substitution of more Fe^{3+} into the crystal structure. The gradients for plagioclase rims and cores in lava samples are very similar, suggesting there is an equal amount of Fe^{3+} throughout the phenocrysts. In contrast, the rims of plagioclase crystals in andesite inclusions have much higher Fe^{3+}, indicating crystallization from a more oxidized melt, allowing the incorporation of Fe^{3+} into the crystal structure. ○ Lava Rims, ● Lava cores, △ Inclusion rims, ▲ Inclusion cores.

rims of plagioclase in dacites and in the cores of plagioclase in andesite inclusions have similar Fe contents, while plagioclase rims in the andesite inclusions have much higher Fe contents (fig. 16). For a given anorthite content, Fe contents may increase as a result of increasing temperature (Bindeman and others, 1998), increasing oxygen fugacity (Phinney, 1992; Wilke and Behrens, 1999; Lundgaard and Tegner, 2004) or increasing melt FeO. The Fe-rich plagioclase rims and Mg-rich orthopyroxene rims from the andesite inclusions are therefore consistent with formation under more oxidizing conditions. We therefore suggest that the andesitic magma underwent a late oxidation event.

As a further test of this hypothesis, Fe^{3+}/Fe^{2+} was estimated for each sample using calculated T and fO_2 and the composition of coexisting orthopyroxene phenocrysts, following Kress and Carmichael (1991). Cores and rims of orthopyroxene phenocrysts are calculated separately, thus giving an indication of the relative redox states of lavas and andesite inclusions (table 5). Both the cores and rims of dacite lavas and the cores of andesite inclusions have similar Fe^{3+}/Fe^{2+} values at ~0.15. In contrast, the orthopyroxene rims in the andesite inclusions return much higher values of Fe^{3+}/Fe^{2+} at ~0.3, suggesting that phenocryst rims in the inclusions crystallized from more oxidized magma than the cores.

The cause of oxidation is difficult to constrain. However, in the dacite lavas, the orthopyroxene microlites and Type 4 phenocrysts rims are more Fe-rich (En_{50-60}) than phenocrysts in both the andesite and the dacite, implying that the last material crystallizing from the dacite is less oxidized than the andesites. This suggests that the main oxidation event occurred during andesite crystallization as these oxidized andesites were then mixed into the dacites only a short time prior to eruption. Oxidation of melt can be caused by significant amounts of hydrogen loss occurring through the degassing of water-rich magmas (Candela, 1997; Burgisser and Scaillet, 2007). Degassing of water-rich andesite melt as it ascended through the crust may therefore have caused the oxidation event.

The location of magma mixing is unclear from the evidence. One possible interpretation is that a magma chamber was located at a depth equivalent to the current deformation anomaly and fed the lavas directly. Another interpretation is that the magma ascended from a deeper source to form a shallower ephemeral magma chamber that supplied eruptions of Uturuncu. Melt H_2O content estimates can be used to constrain depths, using known solubility relationships (for example, Newman and Lowenstern, 2002). The wide range of H_2O (1.4–5.3 wt%) inferred from analyses of melt inclusions in phenocrysts from the dacite may result from leakage, devolatilization or sampling of melt at different pressures during magma ascent (Blundy and Cashman, 2005; Humphreys and others, 2006b). However, assuming H_2O-saturation, they correspond to pressures up to ~ 170 MPa (~6.5 km). Geophysical and petrological evidence for development of shallow magma chambers at depths of 5 to 10 km has been found at several andesite and dacite volcanoes (for example, Nakada and Motomura, 1999; Murphy and others, 2000; Devine and others 2003; Mortazavi and Sparks, 2004; Blundy and Cashman, 2005; Humphreys and others, 2006b) and has also been inferred from the mineral assemblages observed in dacites from the APVC (de Silva and Gosnold, 2007). Stagnation of dacite magmas in the upper crust has been attributed to degassing, crystallization and rheological stiffening of water-saturated andesitic and dacitic magmas (Annen and others, 2006) and location of the brittle-ductile transition (Kavanagh and others, 2006; de Silva and Gosnold, 2007).

HOT ZONE MAGMA GENESIS, PLUTONISM AND VOLCANISM AT UTURUNCU

In this section we interpret the geological, geochronology, petrological, geochemical and geophysical data at Uturuncu within the framework of models of regional Altiplano volcanism and crustal magmatism (Annen and others, 2006, 2008; de Silva

and Gosnold, 2007). The interpretation also incorporates concepts developed by Jackson and others (2003), Jellinek and DePaolo (2003) and Humphreys and others (2006b).

De Silva and Gosnold (2007) have summarized regional data on Cenozoic volcanism (10 Ma to the present) in the Altiplano, which is dominated by eruption of voluminous dacite ignimbrites and caldera formation, with regionally associated andesitic to dacitic stratocones like Uturuncu. Geophysical data demonstrate the existence of a mid-crustal hot zone (the APMB) beneath Uturuncu, where partial melt and magma bodies are present (de Silva, 1989; Chmielowski and others, 1999). Petrological data indicate that dacite magmas derived from the APMB episodically ascends to form shallow magma bodies at 4 to 8 km, which either supply lava eruptions or develop into the very large shallow magma chambers that ultimately erupt catastrophically as ignimbrites with caldera formation. De Silva and Gosnold (2007) develop thermal models of the crust above the APMB assuming that the feature is long-lived. In this model the upper crust is heated so that the brittle-ductile transition is at a shallow level and acts as a mechanical trap for dacite magmas rising from the APMB. The APMB is envisaged as a hot process zone of mushy partially-molten rock through which mantle-derived magmas flux, intrude, partially crystallize at supra-liquidus temperatures and differentiate, accompanied by partial melting of the crust.

Our observations at Uturuncu can be interpreted within the conceptual frameworks of the hot zone model of Annen and others (2006) and regional model of de Silva and Gosnold (2007). Geophysical data indicate that the hot zone may extend into the lower crust (Chmielowski and others, 1999). Deformation models allow a wide range of possible depths as a pressure source for the ongoing uplift. However, all the modeled depths (17−29 km below local surface altitude) are located within the Altiplano-Puna hot zone constrained by geophysical data. The top of this zone is a physically favorable place for magma accumulation because major changes of crust physical properties are anticipated here. Jackson and others (2003) predict that melts within a region of crustal partial melt segregate and migrate upwards to form pools of melt beneath rocks which are impermeable to melt migration due to being below the crustal solidus.

Uturuncu erupted dacite magmas of similar composition over a period of 620 ka, with lavas containing cognate andesite inclusions, norite cumulate xenoliths and crustal xenoliths that have been partially melted. We surmise that andesite magmas are generated by differentiation from basalt precursors much deeper in the lower crust, perhaps accompanied by MASH zone processes as proposed by Hildreth and Moorbath (1988). Andesitic magmas are intruded into the mid-crustal hot zone. Based on the mineral assemblages and melt inclusion data, the andesite magmas parental to the norites and dacites were water-rich with estimated temperatures of 970 to 990°C. A compilation of experimental data on the liquidus phases of andesite compositions (fig. 16 in Annen and others, 2006) indicates that the plagioclase-orthopyroxene assemblage is stable for temperatures <1000 °C and water contents >7 weight percent in the pressure range 300 to 1000 MPa, which is equivalent to the depth range 12 to 40 km for rocks of density 2600 kg/m^3. In agreement with the regional model of de Silva and Gosnold (2007), we interpret the formation of dacite magmas and cognate norite cumulates as occurring by intrusion of andesites into the hot zone and differentiation to form silicic melts. Silicic melts accumulating at the top of the APMB form a major component of the dacite lavas. We interpret the norite adcumulate rocks as residual components of the hot zone that were precipitated from intruding andesite magmas and are complementary to evolved silicic melts that were segregated from the norite residua. The crustal xenoliths likely represent partial melting of crustal rocks trapped as screens in the hot zone. The sillimanite-orthoclase gneiss and igneous quartz-rich

xenoliths are interpreted as refractory rocks from which silicic melt has been extracted. Regional studies of silicic magmas from the Altiplano show that most silicic magmas contain old crustal components (Davidson and others, 1991; Davidson and de Silva, 1992; Feeley, 1993; Feeley and Davidson, 1994; Lindsay and others, 2001).

Prior to 270 ka dacite magmas must have been repeatedly transferred from the top of the APMB into the shallow crust where they formed ephemeral magma chambers that supplied the lava eruptions of the stratovolcano. The brittle-ductile transition in the upper crust is a location of marked rigidity contrast where sills can form to initiate magma chambers (Kavanagh and others, 2006). According to the thermal model of de Silva and Gosnold (2007) this transition is likely located at depths of a few kilometers for crust heated by the APMB over several million years. These depths are also where water-rich silicic magma starts to degas and crystallize (Blundy and Cashman, 2005), and where magma transport is also inhibited by large increases in viscosity (Annen and others, 2006). Magma chambers may also grow into plutons (Glazner and others, 2004; Lipman, 2007; de Silva and Gosnold, 2007).

The petrology and compositions of the dacites together with the water contents inferred from melt inclusions indicate development of shallow open-system magma chambers at a few kms below Uturuncu prior to 270 ka. The dacites were formed by mixing of silicic magma with andesite magma (represented also by inclusions) and disrupted norite cumulates. Quartz, sodic plagioclase ($An_{50\text{-}60}$) that are cores to type 1 phenocrysts, homogeneous type 2 orthopyroxene cores (En_{55}), and biotite are interpreted as phenocrysts suspended in rhyolitic magma bodies in the long periods of dormancy and gradual magma accumulation. Temperatures are likely at the lower end of the spectrum of those found for the dacites (~800°C), noting that the dacites have been variably heated by magma mixing and decompression crystallization (Blundy and others, 2006). Complex textures and disequilibrium in the dacite lavas can be related to magma mixing, decompression related to magma ascent and eruption, and oxidation due to degassing processes.

The volcanic history of Uturuncu provides constraints about several processes in the hot zone. We have identified about 50 lavas from mapping (fig. 4) with volumes that range between 0.1 and 10 km^3. Although some lavas are buried it seems unlikely that the total number of lavas in the edifice exceeds 100 and, for a volume of 85 km^3, the mean lava volume would be ~1 km^3. It is also likely that some eruptions would form several lava flows. Thus the mean repose period would have been much more than 10,000 years with very short eruptive bursts of activity with several lava eruptions within a narrow time window. The most recent period of dormancy has lasted 270 ka. Similar short-lived pulses of volcanism separated by prolonged periods of dormancy have been identified at the andesite volcanism in the Soufrière Hills Volcano Montserrat (Harford and others, 2002; Le Friant and others, 2008). In the long periods of dormancy between eruptions, wet andesite magma differentiated to silicic magmas in APMB. Dormant periods of tens of thousands of years are consistent with the models developed by Jackson and others (2003) for silicic melt extraction by compaction in regions of crustal partial melt and magma accumulation.

The observations at Uturuncu can also be related to models of magma chamber growth and eruption proposed by Jellinek and DePaolo (2003). They proposed that there are two physical regimes for magma chamber evolution in the crust. In one regime, for relatively small magma chambers, the magma supply rate is sufficient to deform the surrounding rocks elastically and reach a failure condition when a dike forms and magma reaches the surface. In this case the volcano erupts repeatedly and the chamber cannot grow to a volume where a caldera forming eruption can occur. In the other regime, for relatively large magma chambers, the surrounding rocks deform in the ductile regime and pressure cannot build up to the threshold for dike

formation. In this case large volumes of magma can accumulate and volumes of magma, tens to thousands of km^3, can accumulate without eruption. Eventually other failure mechanisms might result in a large magnitude caldera-forming eruption or a pluton might grow and consolidate without eruption. The threshold between these two regimes depends on crustal rheology, temperature and magma supply rate. The lava eruptions at Uturuncu can be assigned to the first regime, while the caldera systems of the Altiplano can be assigned to the second regime (de Silva and Gosnold, 2007).

The critical question at Uturuncu is how the current deformation and seismic unrest fits into these conceptual models and what the implications are for future activity. Is it part of a new build up to another lava eruption or even a caldera-forming eruption or does it represent the benign growth of a deep plutonic complex with no implication that Uturuncu will be active again? Many ignimbrite eruptions with volumes of hundreds to a few thousand km^3 have occurred in the Altiplano and Puna regions over the last 10 Ma (de Silva, 1989; Mason and others, 2004; de Silva and others, 2006). However, the existence of a contemporary shallow magma chamber below Uturuncu is not demonstrated from our observations. Prior to 270 ka such chambers may have formed, but never developed to a size sufficient for a large ignimbrite eruption. The current unrest appears to be the consequence of deep intrusion at the top of the APMB.

Consideration of volumes, volume fluxes and the long period of dormancy are intriguing. We generously assume that Uturuncu has erupted 170 km^3 during its lifetime (twice the extant volume), which gives a magma eruption rate of less than 2.7×10^{-4} km^3/yr over 620 ka. This value is more than a factor of 10 less than the mean value of 4×10^{-3} km^3/yr for rhyolitic volcanoes (White and others, 2006) and a factor of about 3 less than the regional rate of 10^{-3} km^3/yr estimated by de Silva and Gosnold (2007). In contrast the current intrusion rate is estimated at approximately 10^{-2} km^3/yr, which is comparable to rates of lava extrusion during historic eruptions of active andesite and dacite dome eruptions (Melnik and Sparks, 2005) and at the high end of the peak intrusion rates estimated by de Silva and Gosnold (2007) for the episodic growth of individual shallow magma chambers in the APVC. The low time averaged rate of Uturuncu might indicate that a significant proportion of the magma has been intruded but not erupted, while the very high current rate inferred from the deformation reflects a short episode of high magma intrusion rate. If the time-average rate were at the regional average value of 10^{-3} km^3/yr, then over 270 km^3 of magma would have accumulated below Uturuncu in the last 270 ka, while 2700 km^3 would have accumulated at the observed intrusion rate.

A key issue is whether there is also a shallow magma chamber or the high rate of deep intrusion could soon lead to the ascent of a large volume of magma to a shallow level. It is certainly possible that the deformation signal of a shallow magma chamber could be disguised by the larger signal of the APMB. Alternatively one may exist but the transfer of magma from the APMB is yet to occur, but might be imminent. Given the enormity of the global hazard of another large caldera-forming eruption on the Earth, there is a strong case that Uturuncu deserves more detailed investigation.

ACKNOWLEDGMENTS

We thank Nick Marsh of Leicester Geology Department for help with XRF analyses, Dr. Stuart Kearns and Dr. John Wade for their assistance in electron microprobe and SEM techniques and Professor Jon Blundy for suggestions and improvements. This study used ERS and Envisat SAR imagery acquired under a Category 1 research project from the European Space Agency. We acknowledge the help of Catherine Annen and Anne Le Friant in the field. We thank Guy Tytgat and Jackie Caplan-Auerbach for assistance in preparing the portable seismic system and

software to extract and view the data, and John Sanchez for assistance with examining data from the PASSCAL seismic stations. Todd Feeley is thanked for generously allowing us to use his diagrams in figures 1 and 2 and for helpful comments on an earlier draft of the paper. We thank Dennis Geist and Wendy Bohrson for helpful and constructive reviews..

REFERENCES

Ague, J. J., Baxter, E. F., and Eckert, J. O., Jr., 2001, High f_{O_2} During Sillimanite Zone Metamorphism of Part of the Barrovian Type Locality, Glen Clova, Scotland: Journal of Petrology, v. 42, p. 1301–1320, doi:10.1093/petrology/42.7.1301.

Alexandre, P., Hamilton, D., and Barford, D., 2006, The ARGUS multicollection noble gas mass spectrometer: Geochimica et Cosmochimca Acta, v. 70, p. A8, doi:10.1016/j.gca.2006.06.1574.

Allmendinger, R. W., Jordan, T. E., Kay, S. M., and Isacks, B. L., 1997, The Evolution of the Altiplano-Puna Plateau of the Central Andes: Annual Review of Earth and Planetary Science Letters, v. 25, p. 139–174, doi:10.1146/annurev.earth.25.1.139.

Andersen, D. J., Lindsley, D. H., and Davidson, P. M., 1993, QUILF: a PASCAL program to assess equilibria among Fe-Mg-Ti oxides, pyroxenes, olivine and quartz: Computers and Geosciences, v. 19, p. 1333–1350, doi:10.1016/0098-3004(93)90033-2.

Anderson, A. T., 1976, Magma mixing: petrological process and volcanological tool: Journal of Volcanology and Geothermal Research, v. 1, p. 3–33, doi:10.1016/0377-0273(76)90016-0.

Annen, C., Blundy, J. D., and Sparks, R. S. J., 2006, The genesis of intermediate and silicic magmas in deep crustal hot zones: Journal of Petrology, v. 47, p. 505-539, doi:10.1093/petrology/egi084.

——— 2008, The sources of granitic magmas in deep hot zones: Transactions of the Royal Society of Edinburgh, v. 97, p. 297–309.

Arculus, R. J., and Wills, K. J. A., 1980, The Petrology of Plutonic Blocks and Inclusions from the Lesser Antilles Island Arc: Journal of Petrology, v. 21, p. 743–799.

Bacon, C. R., and Hirschmann, M. M., 1988, Mg/Mn partitioning as a test for equilibrium between coexisting Fe-Ti oxides: American Mineralogist, v. 73, p. 57–61.

Bindeman, I. N., Davis, A. M., and Drake, M. J., 1998, Ion microprobe study of plagioclase-basalt partition experiments at natural concentration levels of trace elements: Geochimica et Cosmochimica Acta, v. 62, p. 1175–1193.

Blundy, J. D., and Cashman, K., 2005, Rapid decompression-driven crystallization recorded by melt inclusions from Mount St Helens volcano: Geology, v. 33, p. 793–796, doi:10.1130/G21668.1.

Blundy, J., Cashman, K., and Humphreys, M., 2006, Magma heating by decompression-driven crystallization beneath andesite volcanoes: Nature, v. 443, p. 76–80, doi:10.1038/nature05100.

Bonafede, M., Dragoni, M., and Quareni, F., 1986, Displacement and stress fields produced by a centre of dilation and by a pressure source in a viscoelastic half-space: Application to the study of ground deformation and seismic activity at Campi Felgrei, Italy: Geophysical Journal of the Royal Astronomical Society, v. 87, p. 455–485.

Burgisser, A., and Scaillet, B., 2007, Redox evolution of a degassing magma rising to the surface: Nature, v. 445, p. 194–197, doi:10.1038/nature05509.

Cahill, T., and Isacks, B. L., 1992, Seismicity and Shape of the Subducted Nazca Plate: Journal of Geophysical Research, v. 97, No. B12, p. 17503–17529, doi:10.1029/92JB00493.

Candela, P. A., 1997, A Review of Shallow, Ore-related Granites: Textures, Volatiles and Ore Metals: Journal of Petrology, v. 38, p. 1619–1633.

Carroll, M. R., and Rutherford, M. J., 1987, The stability of igneous anhydrite: experimental results and implications for sulfur behavior in the 1982 El Chichon trachyandesite and other evolved magmas: Journal of Petrology, v. 28, p. 781–801, doi:10.1093/petrology/28.5.781.

Carta Geologica De Bolivia, 1996: Geological Survey of Bolivia.

Chmielowski, J., Zandt, G., and Haberland, C., 1999, The central Andean Altiplano-Puna magma body: Geophysical Research Letters, v. 26, p. 783–786, doi:10.1029/1999GL900078.

Clynne, M. A., 1999, A complex magma mixing origin for rocks erupted in 1915, Lassen Peak, California: Journal of Petrology, v. 40, p. 105–132.

Coira, B., Kay, S. M., and Viramonte, J., 1993, Upper Cenozoic magmatic evolution of the Argentine Puna – a model for changing subduction zone geometry: International Geology Review, v. 35, p. 677–720.

Costa, F., Scaillet, B., and Pichavant, M., 2004, Petrological and Experimental Constraints on the Pre-Eruption Conditions of Holocene Dacite from Volcan San Pedro and the Importance of Sulphur in Silicic Subduction-related Magmas: Journal of Petrology, v. 45, p. 855–881, doi:10.1093/petrology/egg114.

Couch, S., Sparks, R. S. J., and Carroll, M. R., 2001, Mineral disequilibrium in lavas explained by convective self-mixing in open magma chambers: Nature, v. 411, p. 1037–1039, doi:10.1038/35082540.

Davidson, J. P., and de Silva, S. L., 1992, Volcanic Rocks from the Bolivian Altiplano: Insights into crustal structure, contamination and magma genesis in the central Andes: Geology, v. 20, p. 1127–1130, doi:10.1130/0091-7613(1992)020<1127:VRFTBA>2.3.CO;2.

Davidson, J. P., Harmon, R. S., and Worner, G., 1991, The source of central Andean magmas; some considerations, *in* Harmon, R. S., and Rapela, C. W., editors, Andean Magmatism and its Tectonic Setting: Geological Society of America Special Paper, v. 265, p. 233–244.

de Silva, S. L., 1989, Altiplano-Puna volcanic complex of the central Andes: Geology, v. 17, p. 1102–1106, doi:10.1130/0091-7613(1989)017<1102:APVCOT>2.3.CO;2.

de Silva, S. L., and Francis, P. W., 1991, Volcanoes of the Central Andes: New York, Springer-Verlag, 216 p.
de Silva, S. L., and Gosnold, W. D., 2007, Episodic construction of batholiths: insights from spatiotemporal development of an ignimbrite flare-up: Journal of Volcanology and Geothermal Research, v. 167, p. 320-335, doi:10.1016/j.jvolgeores.2007.07.015.
de Silva, S. L., Zandt, G., Trumbell, R., Viramonte, J., Salas, G., and Jimenez, N., 2006, Large ignimbrite eruptions and volcano-tectonic depressions in the Central Andes: a thermomechanical perspective: London, Geological Society Special Publication, v. 269, p. 47–63.
Devine, J. D., Gardner, J. E., Brack, H. P., Layne, G. D., and Rutherford, M. J., 1995, Comparison of microanalytical methods for estimating H_2O contents of silicic volcanic glasses: American Mineralogist, v. 80, p. 319–328.
Devine, J. D., Rutherford, M. J., Norton, G. E., and Young, S. R., 2003, Magma Storage Region Processes Inferred from Geochemistry of Fe-Ti Oxides in Andesitic Magma, Soufrière Hills Volcano, Montserrat, W.I.: Journal of Petrology, v. 44, p. 1375–1400, doi:10.1093/petrology/44.8.1375.
Dieterich, J. H., and Decker, R. W., 1975, Finite Element Modeling of Surface Deformation Associated With Volcanism: Journal of Geophysical Research, v. 80, p. 4094–4102, doi:10.1029/JB080i029p04094.
du Bray, E. A., Ludington, S., Brooks, W. E., Gamble, B. M., Ratte, J. C., Richter, D. H., and Soria-Escalante, E., 1995, Compositional characteristics of Middle to Upper Tertiary volcanic rocks of the Bolivian Altiplano: US Geological Survey Bulletin, (200) E no. 2119, 30 p.
Elliott, T., Plank, T., Zindler, A., White, W., and Bourdon, B., 1997, Element transport from slab to volcanic front of the Mariana arc: Journal of Geophysical Research, v. 102, No. B7, p. 14991–15019, doi:10.1029/97JB00788.
Feeley, T. C., 1993, Crustal modification during subduction-zone magmatism: Evidence from the southern Salar de Uyuni region (20°-22°S) central Andes: Geology, v. 21, p. 1019–1022, doi:10.1130/0091-7613(1993)021<1019:CMDSZM>2.3.CO;2.
Feeley, T. C., and Davidson, J. P., 1994, Petrology of Calc-Alkaline Lavas at Volcán Ollagüe and the Origin of Compositional Diversity at Central Andean Stratovolcanoes: Journal of Petrology, v. 35, p. 1295–1340, doi:10.1093/petrology/35.5.1295.
Fialko, Y., Khazan, Y., and Simons, M., 2001, Deformation due to a pressurized horizontal circular crack in an elastic half-space, with applications to volcano geodesy: Geophysical Journal International, v. 146, p. 181–190, doi:10.1046/j.1365-246X.2001.00452.x.
Gill, J. B., 1981, Orogenic Andesites and Plate Tectonics: Berlin, Springer Verlag, 390 p.
Ginibre, C., Wörner, G., and Kronz, A., 2002, Minor- and trace-element zoning in plagioclase: implications for magma chamber processes at Parinacota volcano, northern Chile: Contributions to Mineralogy and Petrology, v. 143, p. 300–315, doi:10.1007/s00410-002-0351-z.
Glazner, A. F., Bartley, J. M., Coleman, D. S., Gray, W., and Taylor, R. Z., 2004, Are plutons assembled over millions of years by amalgamation from small magma chambers?: GSA Today, v. 14, p. 4–11, doi:10.1130/1052-5173(2004)014<0004:APAOMO>2.0.CO;2.
Harford, C. L., Pringle, M. S., Sparks, R. S. J., and Young, S. R., 2002, The volcanic evolution of Montserrat using $^{40}Ar/^{39}Ar$ geochronology, *in* Druitt, T. H., and Kokelaar, B. P., editors, The eruption of the Soufrière Hills Volcano, Montserrat 1995 to 1999: London, Geological Society, Memoir 21, p. 93–113.
Harmon, R. S., and Hoefs, J., 1984, Oxygen isotope ratios in Andean Volcanics, *in* Harmon, R. S., and Barreiro, B. A., editors, Andean Magmatism: Chemical and Isotopic Constraints: Nantwich, United Kingdom, Shiva, p. 9–20.
Harvey, P. K., Lovell, M. A., Brewer, T. S., Locke, J., and Mansley, E., 1996, Measurement of thermal neutron cross absorption section in selected geochemical reference materials: Geostandards Newsletter, v. 20, p. 79–85, doi:10.1111/j.1751-908X.1996.tb00174.x.
Hildreth, W. S., and Moorbath, S., 1988, Crustal contributions to arc magmatism in the Andes of Central Chile: Contributions to Mineralogy and Petrology, v. 98, p. 455–489, doi:10.1007/BF00372365.
Humphreys, M. C. S., Kearns, S., and Blundy, J. D., 2006a, SIMS investigation of electron-beam damage to hydrous rhyolitic glasses: implications for melt inclusion analysis: American Mineralogist, v. 91, p. 667–679, doi:10.2138/am.2006.1936.
Humphreys, M. C. S., Blundy, J. D., and Sparks, R. S. J., 2006b, Magma Evolution and Open-system processes at Shiveluch Volcano: insights from phenocryst zoning: Journal of Petrology, v. 47, p. 2303–2334, doi:10.1093/petrology/egl045.
Jackson, M. D., Cheadle, M. J., and Atherton, M. P., 2003, Quantitative modeling of granitic melt generation and segregation in the continental crust: Journal of Geophysical Research, v. 108, Art. No. 2332, doi:10.1029/2001JB001050.
Jellinek, A. M., and DePaolo, D. J., 2003, A model for the origin of large silicic magma chambers: precursors of large caldera-forming eruptions: Bulletin of Volcanology, v. 65, p. 363–381, doi:10.1007/s00445-003-0277-y.
Johnson, D. J., Sigmundsson, F., and Delaney, P. T., 2000, Comment on "Volume of magma accumulation or withdrawal estimated from surface uplift or subsidence, with application to the 1960 collapse of Kilauea volcano" by P. T. Delaney and D. F. McTigue: Bulletin of Volcanology, v. 61, p. 491–493, doi:10.1007/s004450050006.
Johnson, M. C., and Rutherford, M. J., 1989, Experimentally determined conditions in the Fish Canyon Tuff, Colorado, magma chamber: Journal of Petrology, v. 30, p. 711–737, doi10.1007/s004450050006.
Kavanagh. J., Menand, T., and Sparks, R. S. J., 2006, An experimental investigation of sill formation and propagation in layered elastic media: Earth and Planetary Sciences Letters, v. 245, p. 799–813, doi:10.1016/j.epsl.2006.03.025.
Kay, S. M., Mpodzis, C., and Coria, B., 1999, Neogene magmatism, tectonism, and mineral deposits of the Central Andes (22° to 33°S latitude), *in* Skinner, B. J., editor, Geology and Ore deposits of the Central Andes: Society of Economic Geologists Special Publication, v. 7, p. 27–59.

Kress, V. C., and Carmichael, I. S. E., 1991, The compressibility of silicate liquids containing Fe_2O_3 and the effect of composition, temperature, oxygen fugacity and pressure on their redox states: Contributions to Mineralogy and Petrology, v. 108, p. 82–92, doi:10.1007/BF00307328.

Kussmaul, S., Hörmann, P. K., Ploskonka, E., and Subieta, T., 1977, Volcanism and structure of southwestern Bolivia: Journal of Volcanology and Geothermal Research, v. 2, p. 73–111, doi:10.1016/0377-0273(77)90016-6.

Le Friant, A., Lock, E. J., Hart, M. B., Boudon, G., Sparks, R. S. J., Leng, M. J., Smart, C. W., Komorowski, J. C., Deplus, C., and Fisher, J. K., 2008, Late Pleistocene tephrochronology of marine sediments adjacent to Montserrat, lesser Antilles volcanic arc: London, Journal of the Geological Society, v. 165, p. 279–289, doi:10.1144/0016-76492007-019.

Lee, W. H. K., Bennett, R. E., and Meagher, K. L., 1972, A Method of Estimating Magnitude of Local Earthquakes from Signal Duration: U.S. Geological Survey Open-File Report, n. 28, p., 1972.

Leidig, M., and Zandt, G., 2003, Modeling of highly anisotropic crust and application to the Altiplano-Puna volcanic complex of the central Andes: Journal of Geophysical Research, v. 108, doi:10.1029/2001JB000649.

Lindsay, J. M., Schmitt, A. K., Trumbull, R. B., de Silva, S. L., Siebel, W., and Emmermann, R., 2001, Magmatic Evolution of the La Pacana Caldera System, Central Andes, Chile: Compositional Variation of Two Cogenetic, Large-Volume Felsic Ignimbrites: Journal of Petrology, v. 42, p. 459–486, doi:10.1093/petrology/42.3.459.

Lipman, P. W., 2007, Incremental assembly and prolonged consolidation of Cordilleran magma chambers: Evidence from the Southern Rocky Mountain volcanic field: Geosphere, v. 3, p. 42–70, doi: 10.1130/GES00061.1.

Ludwig, K. R., 2003, Mathematical-Statistical treatment of Data and Errors for ^{230}Th-/U geochronology, *in* Bourdon, B., Henderson, G., Lundstrom, C., and Turner, S., editors, Uranium-Series Geochemistry: Reviews in Mineralogy and Geochemistry, v. 52, p. 631–656.

Luhr, J. F., and Carmichael, I. S. E., 1980, The Colima Volcanic Complex, México: Part I. Post-caldera andesites from Volcán Colima: Contributions to Mineralogy and Petrology, v. 71, p. 343–372.

Lundgaard, K. L., and Tegner, C., 2004, Partitioning of ferric and ferrous iron between plagioclase and silicate melt: Contributions to Mineralogy and Petrology, v. 147, p. 470–483, doi:10.1007/s00410-004-0568-0.

Lundgren, P., Usai, S., Sansosti, E., Lanari, R., Tesauro, M., Fornaro, G., and Berardino, P., 2001, Modeling surface deformation with synthetic aperture radar interferometry at Campi Flegrei caldera: Journal of Geophysical Research, v. 106, B9, p. 19,355–19,367, doi:10.1029/2001JB000194.

Marsh, S. P., Richter, D. H., Ludington, S., Soira-Escalante, E., and Escobar-Diaz, A., 1992, Geologic map of the Alitplano and Cordillera Occidental, Bolivia, *in* Mineral resources of the Altiplano and Cordillera Occidental, Bolivia: U.S. Geological Survey Bulletin 1975.

Mason, B. G., Pyle, D. M., and Oppenheimer, C., 2004, The size and frequency of the largest explosive eruptions: Bulletin of Volcanology, v. 66, p. 735–748, doi:10.1007/s00445-004-0355-9.

Mayel Sunagua, C., 2002, Riesgo Volcánico en el Área del Volcán Uturuncu-Región Sud Lipez del Departamento de Potosí: Tesis de Grado, Univesidad Tomas Frías, Potosí, Bolivia.

McNutt, S. R., 2005, Volcanic Seismology: Annual Review of Earth and Planetary Sciences, v. 33, p. 461–491, doi: 10.1146/annurev.earth.33.092203.122459.

Melnik, O., and Sparks, R. S. J., 2005, Controls on conduit magma flow dynamics during lava dome building eruptions: Journal of Geophysical Research, v. 110, B022, doi:10.1029/2004JB003183, p. 1–21.

Miyashiro, A., 1974, Volcanic rock series in island arcs and active continental margins: American Journal of Science, v. 274, p. 321–355.

Mortazavi, M., and Sparks, R. S. J., 2004, Origin of rhyolite and rhyodacite lavas and associated mafic inclusions of Cape Akrotiri, Santorini: the role of wet basalt in generating calcalkaline silicic magmas: Contributions to Mineralogy and Petrology, v. 146, p. 397–413, doi:10.1007/s00410-003-0508-4.

Murphy, M. D., Sparks, R. S. J., Barclay, J., Carroll, M. R., and Brewer, T. S., 2000, Remobilisation of andesite magma by intrusion of Mafic Magma at the Soufrière Hills Volcano, Montserrat, West Indies: Journal of Petrology, v. 41, p. 21–42, doi:10.1093/petrology/41.1.21.

Nakada, S., and Motamura, Y., 1999, Petrology of the 1991–1995 eruption at Unzen: effusion pulsation and groundmass crystallization: Journal of Volcanology and Geothermal Research, v. 89, p. 173–196, doi:10.1016/S0377-0273(98)00131-0.

Nelson, S. T., and Montana, A., 1992, Sieve-textured plagioclase in volcanic rocks produced by rapid decompression: American Mineralogist, v. 77, p. 1242–1249.

Newman, S., and Lowenstern, J. B., 2002, VOLATILECALC: a silicate melt-H_2O-CO_2 solution model written in Visual Basic for excel: Computers and Geosciences, v. 28, p. 597–604, doi:10.1016/S0098-3004(01)00081-4.

Phinney, W. C., 1992, Partition coefficients for iron between plagioclase and basalt as a function of oxygen fugacity: Implications for Archean and lunar anorthosites: Geochimica et Cosmochimica Acta, v. 56, p. 1885–1895, doi:10.1016/0016-7037(92)90318-D.

Pritchard, M. E., and Simons, M., 2002, A satellite geodetic survey of large-scale deformation of volcanic centres in the central Andes: Nature, v. 418, p. 167–171, doi:10.1038/nature00872.

——— 2004, An InSAR-based survey of volcanic deformation in the central Andes: Geochemistry Geophysics Geosystems, v. 5, 10.1029/2003GC000610.

Renne, P., Karner, B., and Ludwig, K. R., 1998, Radiosotope Dating: Enhanced: Absolute ages aren't exactly: Science, v. 282, p. 1840–1841, doi:10.1126/science.282.5395.1840.

Richards, J. P., and Villeneuve, M., 2002, Characteristics of late Cenozoic volcanism along the Archibarca lineament from Cerro Llullaillco to Corrida de Cori, northwest Argentina: Journal of Volcanology and Geothermal Research, v. 116, p. 161–200, doi:10.1016/S0377-0273(01)00329-8.

Scaillet, B., and Evans, B. W., 1999, The 15 June 1991 Eruption of Mount Pinatubo. I. Phase Equilibria and Pre-eruption P–T–fO_2–fH_2O Conditions of the Dacite Magma: Journal of Petrology, v. 40, p. 381–411, doi:10.1093/petrology/40.3.381.

Schilling, F. R., Partzsch, G. M., Brasse, H., and Schwarz, G., 1997, Partial melting below the magmatic arc in the central Andes deduced from geoelectromagnetic field experiments and laboratory data: Physics of the Earth and Planetary Interiors, v. 103, p. 17–31, doi:10.1016/S0031-9201(97)00011-3.

Schmitz, M., Heinsohn, W. D., and Schilling, F. R., 1997, Seismic, gravity and petrological evidence for partial melt beneath the thickened Central Andean crust (21-23°S): Tectonophysics, v. 270, p. 313–326.

Schmitz, M., Lessel, K., Giese, P., Wigger, P., Araneda, M., Bribach, J., Graeber, F., Grunewald, S., Haberland, C., Lüth, S., Röwer, P., Ryberg, T., and Schulze, A., 1999, The crustal structure beneath the Central Andean forearc and magmatic arc as derived from seismic studies – the PISCO 94 experiment in northern Chile (21° – 23°S): Journal of South American Earth Sciences, v. 12, p. 237–260, doi:10.1016/S0895-9811(99)00017-6.

Sempere, T., Hérail, G., Oller, J., and Bonhomme, M. G., 1990, Late Oligocene-Early Miocene major tectonic crisis and related basins in Bolivia: Geology, v. 18, p. 946–949, doi:10.1130/0091-7613(1990)018<0946:LOEMMT>2.3.CO;2.

Sisson, T. W., and Grove, T. L., 1993, Experimental investigations of the role of H_2O in calc-alkaline differentiation and subduction zone magmatism: Contributions to Mineralogy and Petrology, v. 113, p. 143–166.

Sparks, R. S. J., Sigurdsson, H., and Wilson, L., 1977, Magma mixing: a mechanism for triggering acid explosive eruptions: Nature, v. 267, p. 315–318, doi:10.1038/267315a0.

Stern, C. R., 2004, Active Andean Volcanism: its Geologic and Tectonic Setting: Revista Geológica de Chile, v. 31, p. 161–206.

Tait, S., Jaupart, C., and Vergniolle, S., 1989, Pressure, gas content and eruption periodicity of a shallow, crystallising magma chamber: Earth and Planetary Science Letters, v. 92, p. 107–123, doi:10.1016/0012-821X(89)90025-3.

Thorpe, R. S., 1984, Tectonic setting of active Andean volcanism, *in* Harmon, R. S., and Barreiro, B. A., editors, Andean Magmatism: chemical and isotopic constraints: Cheshire, United Kingdom, Shiva, Ltd. p. 4–8.

Tuttle, O. F., and Bowen, N. L., 1958, Origin of granite in the light of experimental studies in the evolution of granitic magmas in the system $NaAlSi_3O_8$-$KAlSi_3O_8$-SiO_2-H_2O: Geological Society of America Memoir 74, 153 p.

Vernon, R. H., 1985, Possible role of superheated magma in the formation of orbicular granitoids: Geology, v. 13, p. 843–845, doi:10.1130/0091-7613(1985)13<843:PROSMI>2.0.CO;2.

White, S. M., Crisp, J. A., and Spera, F. J., 2006, Long-term volumetric eruption rates and magma budgets: Geochemistry Geophysics Geosystems, v. 7, Q03010, doi:10.1029/2005GC001002, 2006.

Wiemer, S., McNutt, S. R., and Wyss, M., 1998, Temporal and three-dimensional spatial analyses of the frequency-magnitude distribution near Long Valley Caldera, California: Geophysical Journal International, v. 134, p. 409–421, doi:10.1046/j.1365-246x.1998.00561.x.

Wilke, M., and Behrens, H., 1999, The dependence of the partitioning of iron and europium between plagioclase and hydrous tonalitic melt on oxygen fugacity: Contributions to Mineralogy and Petrology, v. 137, p. 102–114, doi:10.1007/s004100050585.

Williams, C. A., and Wadge, G., 1998, The Effects of Topography on Magma Chamber Deformation Models: Application to Mt. Etna and Radar Interferometry: Geophysical Research Letters, v. 25, p. 1549–1552, doi:10.1029/98GL01136.

Yang, X.-M., Davis, P. M., and Dieterich, J. H., 1988, Deformation From Inflation of a Dipping Finite Prolate Spheroid in an Elastic Half-Space as a Model for Volcanic Stressing: Journal of Geophysical Research, v. 93, p. 4249–4257, doi:10.1029/JB093iB05p04249.

Zandt, G., Leidig, M., Chmielowski, J., Baumont, D., and Yuan, X., 2003, Seismic Detection and Characterization of the Altiplano-Puna Magma Body, Central Andes: Pure and Applied Geophysics, v. 160, p. 789–807, doi:10.1007/PL00012557.